Microwaving Mimas, Enceladus, Tethys, Dione, Rhea, Iapetus and Phoebe: Insights into the regolith properties and geological history of Saturn's icy satellites

Alice Le Gall, Léa Bonnefoy, Robin Sultana, Cedric Leyrat, Michael Janssen, Stephen Wall, Emmanuel Lellouch

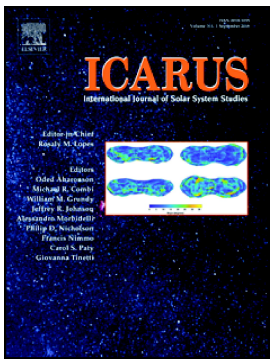

Microwaving Mimas, Enceladus, Tethys, Dione, Rhea, Iapetus and Phoebe: Insights into the regolith properties and geological history of Saturn's icy satellites

A. Le Gall, L.E. Bonnefoy, R. Sultana, C. Leyrat, M.A. Janssen, S. Wall, E. Lellouch

PII: S0019-1035(23)00023-4

DOI: https://doi.org/10.1016/j.icarus.2023.115446

Reference: YICAR 115446

To appear in: *Icarus*

Received date: 28 October 2022

Revised date: 13 January 2023

Accepted date: 24 January 2023

Please cite this article as: A. Le Gall, L.E. Bonnefoy, R. Sultana, et al., Microwaving Mimas, Enceladus, Tethys, Dione, Rhea, Iapetus and Phoebe: Insights into the regolith properties and geological history of Saturn's icy satellites, *Icarus* (2023), https://doi.org/10.1016/j.icarus.2023.115446

Microwaving Mimas, Enceladus, Tethys, Dione, Rhea, Iapetus and Phoebe: Insights into the regolith properties and geological history of Saturn's icy satellites

A. Le Gall[1,2], L.E. Bonnefoy[3,4], R. Sultana[1], C. Leyrat[5], M.A. Janssen[6], S. Wall[6], E. Lellouch[5]

[1] LATMOS/IPSL, UVSQ Université Paris-Saclay, Sorbonne Université, CNRS, Paris, France
[2] Institut Universitaire de France (IUF)
[3] Université Paris-Cité, Institut de physique du globe de Paris (IPGP), CNRS, Paris, France
[4] Cornell Center for Astrophysics and Planetary Science (CCAPS), Cornell University, Ithaca, NY, USA
[5] LESIA, Observatoire de Paris, PSL-Research University, CNRS, Sorbonne Université, Université Paris-Diderot, Paris, France
[6] Jet Propulsion Laboratory, California Institute of Technology, Pasadena, CA, USA,

Corresponding author:

E-mail address: alice.legall@latmos.ipsl.fr

Full postal address:
Alice Le Gall
LATMOS-IPSL – bureau 410
Sorbonne Université
4, place Jussieu
75252 Paris Cedex 05
France

Telephone: +33 6 48 05 46 49

Abstract

While Saturn's main airless moons are all composed largely of water ice, their respective thermal histories and near environments have led to different regolith compositions and structures. Part of this history is recorded in their subsurface which can be probed by microwaves. Using a combined thermal and radiative transfer model, we here investigate all distant observations acquired in the passive mode of the RADAR on board the Cassini spacecraft (2004-2017) at 2.2-cm wavelength. The joint analysis of the derived disk-integrated emissivities and published radar albedos provides new insights into the purity and maturity of the regolith of Saturn's icy moons. We find that satellite-to-satellite variations and large-scale regional anomalies in microwave signatures primarily reflect different degrees of contamination of the regolith by non-ice compounds. To a lesser extent, they may also point to different concentrations of scatterers in the subsurface; these scatterers must be made of ice and/or void rather than of non-ice contaminants. Enceladus appears to have the cleanest regolith likely due to the geological youth of its surface. Observations also suggest that the current heat flux emanating from this moon is not confined to the South Pole Terrain. In the inner system, the degree of purity of the satellites' regoliths decreases from Enceladus outward likely due to the decrease of the E-ring influx. In the outer system, Phoebe's ring mantles Iapetus' leading hemisphere with a decimetric layer of optically-dark and microwave-absorbent dust. Dione is surprisingly less radar-bright and more emissive than expected from both the observed general trend and the current understanding of its geological history. Another question remains outstanding: why are Saturnian moons, and to a lesser extent Jovian moons, so radar-bright at centimetric wavelengths? Current models assuming purely-random scattering in their subsurface fail to simultaneously reproduce active and passive microwave observations, especially for Saturn's inner moons. This may be due the presence of organized and especially efficient backscattering structures in their subsurface. The challenge is now to identify structures that are geologically plausible.

Graphical abstract

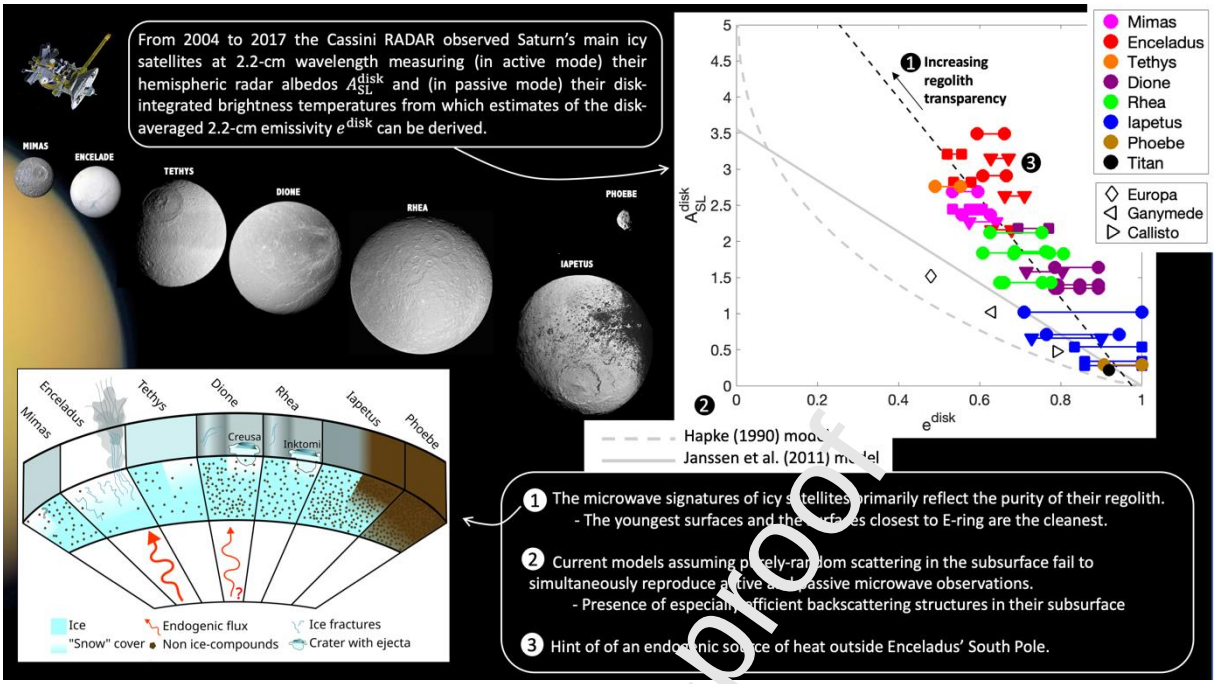

1. Introduction

After Titan, the six largest Saturnian satellites are, in order of distance from Saturn: Mimas, Enceladus, Tethys, Dione, Rhea and Iapetus (Table 1). Phoebe and Hyperion are smaller and exhibit irregular shapes and non-synchronous rotation. The collective formation of these moons and subsequent evolution remains an outstanding problem. All of them are composed largely of water ice (Table 1, Clark et al., 1986; Charnoz et al., 2012). However, their respective thermal histories and near environments have led to different regolith compositions and structures. In particular, they show evidence of varying degrees of geologic activity in the past and, in the case of Enceladus, the present (Porco et al., 2006). The subsurfaces of Saturn's moons contain a record of their thermal and dynamical history; probing them with microwaves provides insights into the various physical and geological processes that have affected them, both into what they have in common and what separates them.

Microwave observations of Saturnian airless satellites are rare and recent. Until the 2004 through 2007 oppositions of the Saturn system, Earth-based radar measurements in the outer solar system were limited to the Galilean satellites and Titan (Muhleman et al. 1990; 1994, Campbell et al. 2003). Black et al. (2004, 2007) observed both hemispheres of Iapetus and the mid-sized Saturnian satellites Rhea, Dione, Tethys and Enceladus with the Arecibo Observatory's 12.6-cm wavelength (2.38 GHz, S-band) radar system. The other Earth-based planetary radar system, Goldstone—equipped with a 3.5 cm transmitter (X-band)—has not yet been used to observe these objects or other Saturnian airless satellites yet. In addition, passive microwave observations of Saturnian moons from Earth are difficult to make due to contamination by emissions from the planet, associated to large instrumental beams, the faintness of some targets, and their small apparent size. That is the reason why they have not been generally conducted. The exceptions are Titan which is large enough (Jaffe et al., 1979; 1980; Grossman and Mulheman, 1992; Butler and Gurwell, 2004), Iapetus, which, at maximum elongation, is far enough from Saturn as viewed from the Earth (Ries, 2012; Hagen et al., 2014; Bonnefoy et al., 2020a) and, very recently, Phoebe despite its small size but thanks to its large distance to Saturn and the advances in radio-interferometry (Bonnefoy, 2020). In that regard, the Cassini RADAR (active and passive) observations of Saturn's icy moons are unique.

The Cassini mission has explored Saturn's system from 2004 to 2017. The onboard RADAR operating at a wavelength of 2.2 cm (13.78 GHz, Ku-band, Elachi et al., 2004), had been initially designed for the exploration of Titan but also regularly turned its antenna towards the main airless icy satellites of Saturn during. In addition to its active mode, the Cassini RADAR includes a passive (or radiometry) mode designed to record the thermal emission from the targeted surfaces at 2.2-cm. The scientific objectives of Cassini RADAR icy satellite observations were to provide constraints on the thermal, physical and compositional properties of the first few meters (or more, depending on the transparency of the subsurface material) below the surface of the investigated objects and, doing so, gain insights into the degree of purity and maturity (or structural complexity) of their water-ice regolith. This dataset has already brought to light notable differences among Saturn's mid-sized satellites (Ostro et al., 2006; 2010; Le Gall et al., 2019). It has also provided a new wavelength scale to further explore hemispheric dichotomies such as the dramatic two-tone coloration of Iapetus (Le Gall et al., 2014) and revealed regional anomalies including the ejecta blanket of young crater Inktomi on Rhea (Wye, 2011; Bonnefoy et al., 2020b) or the Leading Hemisphere Terrain (LHT, Crow-Willard and Pappalardo, 2015) of Enceladus (Ries and Janssen, 2015). In addition, operations at closer ranges, i.e. spatially-resolved, offered a unique opportunity to examine or detect features of interest at the surface and search for potential "hot spots" in the near-surface as

found near Enceladus's "tiger stripes" (Le Gall et al., 2017). Overall, the Cassini RADAR observations of Saturn's icy moons have greatly enhanced our understanding of the diversity of icy regoliths in the Saturnian System, especially pointing to the key role of the interaction with the dust rings (namely the E-ring and the Phoebe ring, Le Gall et al., 2019).

However, this dataset has not yet been fully analyzed and published yet. Following the analysis of Cassini RADAR active observations of Saturn's icy moons described in Le Gall et al. (2019) and expanding on the work of Ostro et al. (2006; 2010), we present in this paper a comprehensive analysis of the passive RADAR observations of these objects. Most of Cassini RADAR icy satellite observations were distant i.e., occurring at ranges where the antenna beamwidth is comparable to or greater than the apparent angular extent of the target's disk and thus primarily designed to provide disk-integrated quantities: hemispheric-averaged radar albedos in the RADAR active mode and disk-integrated brightness temperatures in the passive mode.

Section 2 describes the calibration and reduction of all available Cassini passive radiometry data. By comparison to a combined thermal and radiative transfer model, these data provide a range of possible values for the disk-averaged 2.2-cm emissivity of each Saturn satellite (section 3). When relevant, observations acquired on the satellite leading sides (which face the direction of motion of the moon in its orbit around Saturn) are separated from observations acquired on their trailing sides. The derived emissivities are then compared to radar albedos measured at the same wavelength and on the same hemispheres (section 4.1) and both datasets are analyzed against commonly invoked emissivity/backscatter models (sections 4.2 and 4.3). These comparisons yield important conclusions on the compositional and structural properties of Saturnian moon regoliths.

Table 1: Characteristics of the main satellites of Saturn.

Satellite	Mean radius[a] (km)	Semi-major axis (R_{Saturn}[b])	Orbital period (days)	Rotation period (days)	Mean density (kg/m^3)	Bulk water ice fraction (%)[c]
Mimas	198.2	3.08	0.94	0.94	1149	89%
Enceladus	252.1	3.94	1.37	1.37	1609	67%
Tethys	531.0	4.89	1.89	1.89	985	97%
Dione	561.4	6.26	2.74	2.74	1478	73%
Rhea	763.5	8.74	4.52	4.52	1237	85%
Titan	2574.7	20.27	15.95	15.95	1879	54%
Hyperion	135.0	24.57	21.28	chaotic	544	Very porous
Iapetus	734.3	59.09	79.33	79.33	1088	91%
Phoebe	106.5	214.8	548.0	0.39	1638	65%

[a] From Thomas (2010) for all satellites except for Titan. From Zebker et al. (2009) for Titan.
[b] R_{Saturn} is Saturn equatorial radius at 1 bar, namely 60 330 km.
[c] These values are estimated assuming a silicate density of 3000 kg/m^3 and a solid ice bulk density of 918 kg/m^3. See also Charnoz et al. (2012).

2. Passive radiometry observations of Saturn's icy satellites

2.1 Data acquisition

In its passive mode, the Cassini RADAR recorded the incoherent thermal emission from the region of the sky encompassed by the antenna beam as a time series of antenna temperature

measurements. Each antenna temperature results from the convolution of the antenna radiation pattern with the distribution of the brightness temperature of the scene observed at a given time. The radiation pattern of the Cassini radiometer consists of a main central beam (mb) with half power beam width (HPBW) of 0.37°, near sidelobes (nsl) out to 2° from the mb axis, and far sidelobes (fsl) (Janssen et al., 2009). The mb and nsl are well known; they were measured during a scan of the Sun performed in 2001. The fsl were not measured but derived from the mapmaking process for Titan assuming circularly symmetric sidelobes.

Cassini radiometry icy satellite observations can be divided into three types (see Fig. 1 in Bonnefoy et al., 2020b):

(1) Distant scans during which the antenna beam was scanned in a rectangular pattern (typically 2° in length) centered on the target and extending off the disk for baseline calibration (see section 2.2). This observing scheme was specifically designed for the derivation of disk-averaged brightness temperature and was performed at ranges between 40,000 km and 400,000 km with long integration time (~1 s). Due to their uniform coverage and off-disk calibration observations, these data yield the most reliable disk-integrated brightness temperatures. Several of these scans were acquired at close enough range for spatially resolved brightness temperatures, but remain distinct from resolved scans because the latter extend off-disk.

(2) The so-called "stares" during which the antenna remained fixed on one or a few points on the target. This observing geometry was primarily intended for the derivation of disk-integrated radar albedos (Le Gall et al., 2019) but passive measurements were performed before active ones or in-between burst cycles generally with a short integration time (<0.3 s). The calibration of this radiometry dataset is challenging and for the purpose of this work we only consider passive measurements acquired before the RADAR transmitter is turned on (that is, before it affects the receiver physical temperature). Furthermore, stares do not have a uniform coverage of the disk, so they provide local rather than disk-integrated temperatures.

(3) Spatially-resolved scans during which both active and passive measurements were collected simultaneously from ranges typically between 5,000 and 100,000 km. During these scans, the transmitter was on but the observation lasted long enough so that the receiver temperature became stabilized; the radiometry dataset can therefore be used as long as it includes contiguous cold sky measurements so that any drift in the radiometer output can be effectively removed.

By the end of the Cassini mission in 2017, radar/radiometry observations of Saturn's icy satellites had been collected during 38 flybys: 4 flybys of Mimas, 10 of Enceladus, 3 of Tethys, 6 of Dione, 9 of Rhea, 3 of Iapetus, 1 of Phoebe and 2 of Hyperion. Putting aside the 2 flybys of Hyperion (Hyperion has a chaotic rotation and thus experiences diurnal temperature variations that are impossible to predict, see Table 1) and unusable radiometry data (due to change in the receiver physical temperature or to the lack of off-disk observations for baseline calibration), this represents a total of 74 observational segments from which disk-integrated brightness temperatures can be derived (see section 2.3) : 41 distant scans, 30 stares and 3 resolved scans.

Table 2 reports the characteristics of each of these segments. Note that some observations, even if classified as "distant" or unresolved, were performed with beam size as small as about 0.3-0.5 satellite diameter. They are thus able to resolve large-scale features at the surface. They

have been processed using an iterative deconvolution technique to produce maps published in Bonnefoy et al. (2020b) and Bonnefoy (2020). However, for this work, we focus on the disk-averaged quantities with the ultimate goal of building a global picture of the variations of the microwave signatures (both in terms of thermal emission and radar albedo) among Saturn's mid-sized satellites.

Table 2: All Cassini icy satellite radiometry observations useful for the derivation of disk-integrated brightness temperatures. Distant scans are identified with a "u" (as in "unresolved"), stares with a "s" and resolved scans with a "r". Only usable data are listed i.e., data perturbed by temperature changes caused by the transmitter being on or not well calibrated due to lack of baseline observation were not considered. The observations noted with a '°°' lack a background baseline at the end of the scan. The derived disk-integrated brightness temperatures are corrected for the CMB (Cosmic Microwave Background).

	Flyby Segment	Date	Start End (UTC)	Beam size Start End (satellite diameter)	Sub-s/c point (Lon (°E), Lat (°N))	Local time at the sub-s/c point (hh:mm)	T_b^{disk} (K)
MIMAS	MI47 2u	2007 JUN 28	03:35:27 04:01:17	3.80-3.95	(-[illegible] 3, -[illegible].3)	11:14	**45.5±1.5**
	MI053 1u	2007 DEC 03	00:31:36 00:56:36	4.77-4.34	(-92.9,15.7)	20:33	**41.3±1.4**
	MI53 2s	2007 DEC 03	01:15:46 01:21:36	4.[illegible]-3.[illegible]3	(-96.9, 16.8)	20:49	**41.6±1.2**
	MI064 2u	2008 APR 11	10:21:17 10:49:37	1.95-2.19	(-163.6, -70.3)	0:10	**44.1±0.7**
	MI126 1u	2010 FEB 13	14:51:[illegible] 15:14:30	0.82-0.72	(96.7, -3.5)	23:32	**44.9±0.5**
	MI126 2s	2010 FEB 13	15:[illegible]:30 15:[illegible]:48	0.72-0.55	(88.7, -5.0)	23:24	**45.7±0.5**
ENCELADUS	EN003 2u	2005 FEB 17	10:[illegible]:29 1[illegible]:20:49	3.01-3.51	(127.6, 0.7)	0:53	**39.0±1.2**
	EN004 1s	2005 MAR 09	12:12:03 12:17:33	0.94-0.97	(-65.1,0.3)	3:18	**35.8±0.4**
	EN004 2u	2005 MAR 09	13:04:23 13:46:17	1.19-1.37	(-74.2, 0.3)	3:38	**34.0±0.5**
	EN028 1s	2006 SEP 10	00:14:23 00:53:39	1.93-2.23	(148.1, 55.1)	17:08	**38.1±1.0**
	EN032 1s	2006 NOV 09	01:44:18 02:21:25	1.16-1.21	(115.2, -27.8)	10:47	**39.9±0.8**
	EN032 2u	2006 NOV 09	02:20:55 02:31:05	1.21-1.25	(113.2, -14.6)	10:51	**39.9±0.5**
	EN050 2u	2007 SEP 30	15:35:03 16:00:46	1.59-1.63	(-131.4, 16.7)	08:04	**31.9±0.8**
	EN061-1 1u	2008 MAR 12	15:11:48 15:36:48	2.46-2.22	(-107.2, 69.2)	1:47	**35.4±0.8**

	EN061-12s°°	2008 MAR 12	15:48:28 16:21:29	2.10-1.77	(-111.8, 69.6)	02:00	**34.1±0.7**
	EN061-21s°°	2008 MAR 12	20:24:37 20:28:52	0.86-0.90	(26.0, -70.8)	14:11	**57.8±1.3**
	EN0881u	2008 OCT 09	11:31:24 11:38:04	4.84-4.80	(-36.0, 66.6)	2:55	**36.7±1.6**
	EN0882u	2008 OCT 09	12:24:44 12:53:04	4.47-4.25	(-42.5, 65.3)	3:20	**38.6±1.2**
	EN0883s°°	2008 OCT 09	12:54:44 13:44:24	4.24-3.82	(-47.4, 64.6)	3:35	**38.1±1.3**
	EN1201u	2009 NOV 02	01:46:02 02:27:42	2.11-1.91	(61.5, -0.7)	23:23	**41.8±0.7**
	EN1202u	2009 NOV 02	02:44:22 03:21:02	1.83-1.62	(55.6, -0.9)	23:40	**41.5±0.7**
	EN15610u	2011 NOV 06	06:32:51 06:46:33	0.54-0.62	(-14.5, -0.8)	10:19	**38.7±0.9**
	EN15611u	2011 NOV 06	06:58:12 07:12:54	0.69-0.78	(-13.5, -0.7)	10:22	**38.3±0.8**
TETHYS	TE0152u	2005 SEP 24	06:50:21 07:21:41	0.87-1.00	(151.8, -0.3)	0:56	**34.3±0.4**
	TE0481s	2007 JUL 20	17:41:31 17:45:45	0.5[illegible]- 0.58	(-109.3, 2.4)	5:15	**31.3±0.3**
DIONE	DI0161s	2005 OCT 11	20:53:27 22:53:00	0.59 -1.04	(-17.7, 0.1)	1:01	**56.8±0.7**
	DI0162u	2005 OCT 11	22:52:1[illegible] 23:30:20	1.04-1.20	(-23.7, 0.2)	1:05	**55.4±0.6**
	DI0163s	2005 OCT 11	23:30:20 2[illegible]:34:30	1.20-1.22	(-25.0, 0.2)	1:06	**55.8±0.7**
	DI0271s	2006 AUG 16	11:26:23 12:11:07	0.99-0.96	(94.1, -31.1)	1:33	**56.6±0.6**
	DI0331s	2006 NOV 21	02:32:06 03:37:45	0.43-0.52	(-0.9, 32.1)	2:43	**56.1±0.6**
	DI0501u	2007 SEP 30	00:19:28 01:12:08	0.69-0.59	(152.5 -13.2)	19:42	**53.5±0.6**
	DI0502s	2007 SEP 30	01:12:08 02:47:37	0.59-0.42	(136.9, -13.0)	18:52	**55.4±0.6**
	DI1631r	2012 MAR 28	02:01:07 03:38:37	0.56-0.34	(-16.7, -0.9)	19:02	**54.7±0.9**
	DI1632u	2012 MAR 28	03:38:37 03:49:22	0.34-0.32	(-36.6, -1.1)	18:47	**55.2±1.4**

	DI163 3s	2012 MAR 28	03:48:37 03:51:37	0.32-0.32	(-39.4, -1.1)	18:43	**57.0±0.6**
	DI177 1s	2012 DEC 23	03:38:37 03:49:22	1.33-1.34	(-96.5, 40.5)	6:33	**46.6±0.7**
	DI177 2u	2012 DEC 23	03:48:37 03:51:37	1.34-1.35	(-95.1, 45.8)	6:41	**47.9±0.6**
	DI177 3u	2012 DEC 23	04:16:06 05:08:10	1.36-1.37	(-93.8, 49.1)	6:55	**47.5±0.6**
RHEA	RH011 1s	2005 JUL 14	08:15:04 09:00:03	0.85-0.81	(-67.6, -77.3)	20:18	**50.2±0.9**
	RH011 2u	2005 JUL 14	09:08:13 09:41:43	0.80-0.78	(-48.2, -74.6)	21:35	**48.0±0.7**
	RH018 2u	2005 NOV 27	04:39:04 05:21:54	0.70-0.79	(-22.2, 0.2)	0:05	**50.0±0.6**
	RH022 2u	2006 MAR 21	11:03:25 12:57:05	0.45-0.57	(-135.1, 0.9)	23:06	**47.4±0.6**
	RH022 3u	2006 MAR 21	13:23:15 14:27:05	0.60-0.67	(-162.1, 0.7)	22:38	**48.1±0.6**
	RH022 4s	2006 MAR 21	15:02:05 15:30:25	0.72-0.75	(-162.1, 0.6)	22:22	**48.3±0.5**
	RH045 1u	2007 MAY 27	11:21:28 11:49:48	0.85-0.83	(-58.0, -44.1)	18:28	**48.2±0.6**
	RH045 2s	2007 MAY 27	11:49:48 13:00:12	0.83-0.79	(-63.9, -45.0)	17:45	**50.1±0.6**
	RH049 1u	2007 AUG 29	20:35:05 20:47:35	0.55-0.47	(15.4, -0.3)	20:38	**50.0±0.6**
	RH127 1u	2010 MAR 02	13:42:57 14:29:32	0.52-0.41	(-159.2, 0.3)	0:05	**47.7±0.6**
	RH127 2u	2010 MAR 02	14:33:37 15:22:32	0.41-0.30	(-162.0,0.4)	0:06	**48.0±0.7**
	RH127 3s	2010 MAR 02	15:22:42 15:24:22	0.30-0.29	(-163.3,0.5)	0:06	**47.2±0.5**
	RH127 4r	2010 MAR 02	15:50:04 16:49:17	0.24-0.11	(-166.7,1.1)	0:05	**50.9±1.3**
	RH177 1u	2012 DEC 22	20:06:51 20:28:41	0.42-0.37	(-102.1,-75.9)	6:12	**44.6±0.7**
	RH177 2u	2012 DEC 22	20:38:31 20:57:16	0.35-0.31	(-91.6, -77.0)	7:06	**45.1±0.7**
IAPETUS	IA00B 1s	2004 DEC 31	04:42:38 05:14:48	0.71-0.70	(-72.9, 38.2)	14:35	**76.2±0.8**

	IA00B 2u	2004 DEC 31	05:13:48 06:27:5	0.70-0.67	(-72.1, 39.8)	14:41	**72.8±0.9**
	IA00B 3s	2004 DEC 31	06:47:59 07:48:43	0.67-0.65	(-70.3, 42.7)	14:49	**73.8±0.8**
	IA00C 1s	2005 JAN 01	14:45:44 19:05:1	0.84-0.95	(58.8, 47.0)	23:55	**58.0±0.9**
	IA00C 2u	2005 JAN 01	19:12:43 20:42:43	0.95-0.99	(60.9, 43.7)	0:00	**58.4±0.7**
	IA00C 3u	2005 JAN 01	20:57:43 22:21:03	1.00-1.04	(61.7, 42.2)	0:04	**58.3±0.7**
	IA00C 4s	2005 JAN 01	22:26:03 22:32:43	1.04-1.04	(62.0, 41.5)	0:04	**59.8±0.6**
	IA017 1s	2005 NOV 12	21:49:07 23:21:19	1.84-1.84	(0.1, 39.4,	18:33	**66.1±1.0**
	IA017 2u	2005 NOV 12	23:21:19 00:04:39	1.84-1.85	(1.3, 39.5,	18:36	**65.0±0.8**
	IA049_1 1u	2007 SEP 09	07:38:32 08:23:32	1.13-1.10	(- 65.4,11.8)	21:52	**77.8±0.9**
	IA049_1 2s	2007 SEP 09	08:26:02 08:47:42	1.10-1.09	(- 65.5,11.8)	21:52	**78.4±0.8**
	IA049_2 1u	2007 SEP 10	00:12:00 01:07:00	0.52-0.48	(-69.3, 11.8)	21:49	**77.4±0.9**
	IA049_2 2s	2007 SEP 10	01:07:00 02:29:43	0.48-0.43	(-69.6, 11.8)	21:48	**80.2±0.8**
	IA049_3 1r	2007 SEP 10	11:19:42 12:17:47	0.11-0.07	(-76.9, 11.3)	21:21	**81.1±1.7**
	IA049_4 2u	2007 SEP 11	03:51:15 04:51:45	0.50-0.54	(106.8, -11.9)	9:54	**62.6±0.8**
PHOEBE	PH002 1u	2004 JUN 11	14:31:11 15:22:31	3.38-2.81	(134.0, -24.6)	6:05	**84.5±1.6**
	PH002 2s	2004 JUN 11	15:22:31 15:34:14	2.81-2.68	(113.0, -24.6)	6:03	**83.7±1.4**
	PH002 3s	2004 JUN 11	21:37:52 00:02:08	1.39-3.00	(12.0, 25.1)	17:56	**77.5±1.5**
	PH002 4u	2004 JUN 11	23:59:09 00:26:26	2.97-3.27	(-48.2, 25.1)	17:56	**78.2±1.8**
	PH002 5u	2004 JUN 12	00:30:34 00:47:06	3.32-3.50	(-64.9, 25.1)	17:54	**76.1±1.9**
	PH002 6s	2004 JUN 12	00:47:16 01:33:09	3.51-4.02	(-84.0, 25.1)	17:45	**83.1±1.9**

2.2 Data calibration

The updated calibration of the Cassini radiometry icy satellite dataset is described in detail in Bonnefoy et al., (2020a) and Bonnefoy (2020). It follows the method developed for Titan by Janssen et al. (2009; 2016) with small adaptation to airless icy satellites (i.e., removal of the absorption factor due to Titan's atmosphere). It takes into account the gain drift with time over

the course of the Cassini mission (-0.30%/year e.g., due to aging of the radiometer components) and includes the subtraction of the far sidelobe contribution and baseline offset. The far-side lobe contribution varies along the observation sequence due to changing range and distance to the limbs but remains small, always smaller than 5% of the signal. It is estimated by fitting simulated temperatures obtained by convolving the radiation beam pattern to a disk of uniform temperature to the measured antenna temperatures (see also Le Gall et al., 2014). The zero level or baseline offset is determined by interpolating empty sky observations (typically at the Cosmic Microwave Background temperature of 2.7 K) that generally precede and follow each scan line or stare.

In the calibration process, pointing and time offsets are corrected. In particular, a systematic antenna pointing offset has been reported in radiometer scans of Saturn's rings (Zhang et al., 2017), Enceladus (Le Gall et al., 2017) and Jupiter (Moeckel et al., 2019). This offset has an angular amplitude of about 0.036° (a tenth of the main beam diameter) which can significantly affect the reduction of poorly resolved dataset. Unfortunately, it has not been corrected in the geometry information included in the Short Burst Data Record (SBDR) publicly available on the Planetary Data System (PDS). Following Zhang et al. (2017), we have re-calculated the geometry of each observation after modifying the RADAR instrument boresight direction in the Cassini frame definitions SPICE kernel to account for this offset (as already done for the Cassini Radio Science Experiment which also used the 4-m communication antenna of the Cassini spacecraft). In addition to this constant beam pointing offset, higher order pointing uncertainties (likely due to uncertainties in the pointing of the Cassini spacecraft) and small errors in the timing of the observations must be corrected. This is done for each observation by including these unknown pointing and timing offsets as parameters in the model used to ultimately derive the disk-integrated brightness temperatures (see details in section 2.3).

Janssen et al. (2009; 2016) estimate that the resulting calibrated antenna temperatures are accurate to ~1%. A random Gaussian noise σ_G inversely proportional to the square root of the integration time must be added to this error. It was determined empirically by Bonnefoy et al., (2020b) and found to be generally small (typically 0.1 K for an integration time of 1 s) compared to the calibration uncertainty. The uncertainty on the measured antenna temperatures T_A thus follows from:

$$\sigma = \sqrt{(0.01T_A)^2 + \sigma_G^2} \quad (1)$$

2.3 Data reduction: disk-integrated brightness temperatures

Once the measured antenna temperatures are calibrated, the thermal emission from the satellite's disk, expressed as its disk-averaged brightness temperature $T_{\mathrm{b}}^{\mathrm{disk}}$, is derived by comparison of the data to a surface brightness temperature reference model that takes into account the geometry of observation and the antenna beam pattern. The data reduction follows an approach similar to the one described in Ostro et al. (2006), Janssen et al. (2009), Le Gall et al. (2014; 2017), Zhang et al. (2017), Moeckel et al. (2019) and Bonnefoy et al. (2020b). Only the chosen reference brightness temperature model T_{b}^{m} is different: we here assume a uniform smooth surface of a given (real) dielectric constant $\varepsilon_{\mathrm{r}}'$ and allow for latitudinal temperature variations when relevant (i.e. when the spatial resolution is high enough).

More specifically, for each data point, the antenna polarization, and pointing direction are calculated using the SPICE/NAIF toolkit (Acton, 1996) and the emissivity is modeled as proposed by Heiles and Drakes (1963):

$$e(\varepsilon'_{\mathrm{r}}) = \left(1 - R_{\parallel}(\varepsilon'_{\mathrm{r}}, \theta)\right)\cos^2\delta + \left(1 - R_{\perp}(\varepsilon'_{\mathrm{r}}, \theta)\right)\sin^2\delta \quad (2)$$

where $R_{\parallel}$ and $R_{\perp}$ are the Fresnel reflection coefficients in, respectively, parallel and perpendicular polarizations for an emission angle of θ and δ is the angle between the parallel polarization direction and the azimuthal position of the observed point at the surface.
The physical temperature is defined to vary with the latitude η as follows:

$$T^m_{\mathrm{phys}}\left(T_{\mathrm{Eq}}, \Delta T\right) = T_{\mathrm{Eq}} - \Delta T\left(\frac{1 - \cos 2\eta}{2}\right) \quad (3)$$

where T_{Eq} is the mean surface temperature at the Equator and ΔT the Equator-to-pole temperature difference (thus assumed symmetric around the Equator and with cooler polar regions). By virtue of the Rayleigh-Jeans approximation which applies in the microwave domain, at each point of the satellite disk, T^m_{b} is simply the product of the emissivity and the physical temperature.

$$T^m_{\mathrm{b}}(\varepsilon'_{\mathrm{r}}, T_{\mathrm{Eq}}, \Delta T) = e(\varepsilon'_{\mathrm{r}}) \times T^m_{\mathrm{phys}}\left(T_{\mathrm{Eq}}, \Delta T\right) \quad (4)$$

This model is convolved with the well-determined radiometer beam pattern within 2° (mb + nsl) along the raster-scan path, allowing for possible timing and pointing offsets (i.e., allowing for a drift in time and a shift of the beam pattern center with respect to what is computed using the SPICE toolkit; see Appendix A in Moeckel et al. (2019) for more details), in order to produce synthetic antenna temperature data with the same viewing geometry as the time-ordered measured data.

The model parameters, namely $\varepsilon'_{\mathrm{r}}$, T_{Eq}, ΔT, the pointing error and the timing offset, are then adjusted to the data until the chi-squared sum of the residuals is minimized using the Levenberg-Marquardt algorithm (Levenberg, 1944; Marquardt, 1963) and all the data collected over the satellite disk, up to one main beam diameter away from the limbs. For unresolved observations (i.e., when angular size of the satellite is smaller than the beam size), the ΔT parameter is set to zero since a model with uniform disk temperature is sufficient for such dataset (for these observations, similar results are actually obtained with ΔT set to zero or variable).

T_b^{disk} is then derived from the best fit brightness temperature model as follows:

$$T_{\mathrm{b}}^{\mathrm{disk}} = \frac{1}{\Omega^{\mathrm{disk}}}\int T^m_{\mathrm{b}}\, d\Omega \quad (5)$$

where Ω^{disk} is the apparent disk solid angle and T_b^m the best-fit modeled brightness temperature of each element of solid angle $d\Omega$.

Table 2 reports the 74 derived disk-integrated brightness temperatures. The results are almost insensitive to the choice of *a priori* model parameters including the value of the dielectric constant. We stress that they are also almost insensitive to our choice of model for T^m_{b}. The estimated error on the derived T_b^{disk} is the quadratic sum of the measurement uncertainty (eq. (1)) and of the reduced chi-squared value χ_r resulting from the fitting process i.e., calculated from the best-fit residual R as follows: $\chi_r = \sqrt{\sum_N R^2/(N-M)}$ where N is the number of data points for a given observational segment and M the number of free parameters of the model (5 or 6).

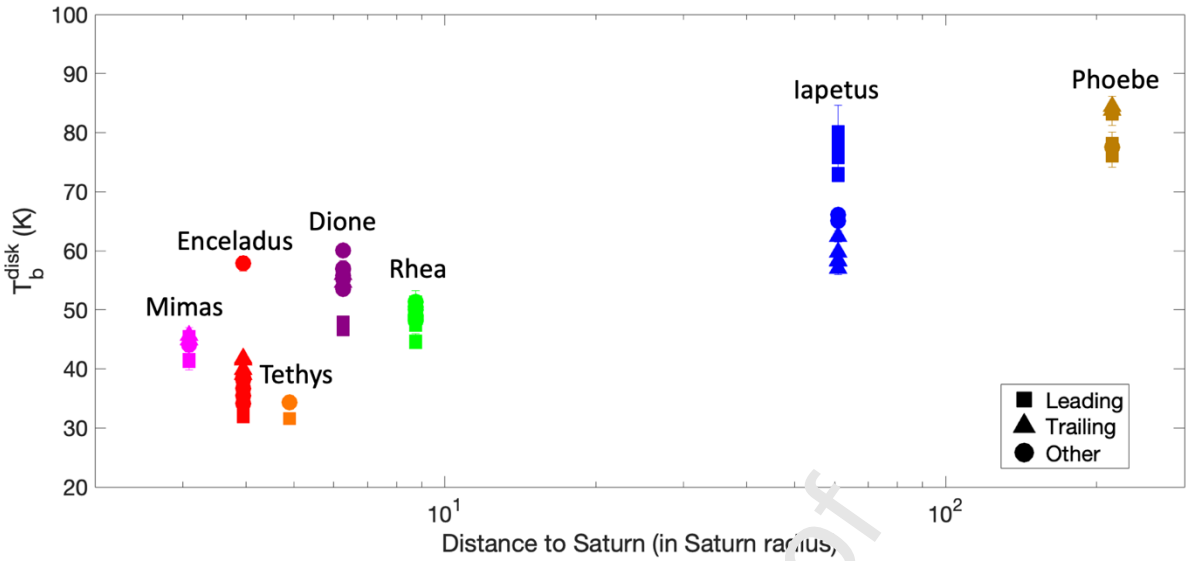

Fig. 1: Derived disk-integrated brightness temperatures of Mimas, Enceladus, Tethys, Dione, Rhea, Iapetus and Phoebe. For each satellite, when available, values are shown separately for the leading (centered at -90°E, 0°N) and trailing sides (centered at 90°E, 0°N). Values are considered as representative of the leading or trailing sides if the sub-spacecraft point is at an angular distance inferior to 45° from their respective center. Otherwise they are indicated as "other".

Fig. 1 compares the disk-integrated brightness temperatures of Mimas, Enceladus, Tethys, Dione, Rhea, Iapetus and Phoebe. It shows clear satellite-to-satellite variabilities with the inner moons, especially Mimas, Tethys and Enceladus, being radiometrically colder than the outer moons Iapetus and Phoebe. These variations are opposite to that of the disk-integrated radar albedos derived from Cassini RADAR active distant observations (Le Gall et al., 2019, see section 4). Both of them likely primarily reflect variations in the degree of volume scattering in the regoliths due to varying contamination by non-ice compounds. Ultra clean subsurfaces are indeed expected to be more radar-bright than dirty ones because they are more favorable to volume scattering. They should concurrently be less emissive inasmuch as volume scattering reduces the outgoing thermal radiation. This will be further discussed in sections 3 and 4.

Fig. 1 also reveals hemispheric dichotomies. The most outstanding of them is observed on Iapetus whose leading side exhibits significantly higher brightness temperatures than its trailing side. We recall that Iapetus is known for its dramatic two-tone coloration in the optical domain; its trailing side and poles are about an order of magnitude optically brighter than most of its leading hemisphere. It is now generally admitted that this albedo dichotomy is mainly due to the exogenic deposition, on the leading side, of dark materials originating from the vast debris ring from Phoebe (Buratti et al., 2002; Verbiscer et al., 2009; Dalle Ore et al., 2012). The presence of an optically dark contaminant at the surface can both lead to high physical temperatures (due to the low albedo) and a large surface emissivity at 2.2-cm (if the dark contaminant is also a microwave absorbent and is present at depths of at least one to several decimeters) therefore explaining the high T_b^{disk} values recorded on the leading hemisphere of Iapetus.

Though less pronounced than that of Iapetus, Enceladus also exhibits a leading/trailing asymmetry which is not apparent in active RADAR Cassini observations (Le Gall et al., 2019): its leading side is radiometrically colder than its trailing side. Ries and Janssen (2015) advance

that is due to a large-scale emissivity anomaly (rather than a thermal inertia anomaly), spatially correlated with the so-called "Leading Hemisphere Terrain" (LHT). The geological youth of this terrain suggests the presence of ultra-clean water ice in the near-subsurface, likely extruded from the interior during a relatively recent period of activity, which would explain why it is significantly (about 30%) less emissive at 2.2-cm than its surrounding.

Fig. 1 also suggests that the leading hemispheres of Tethys, Dione and Rhea are less emissive than the rest of their surface (squared markers). This would be consistent with dynamical models which predict the deposition, on these hemispheres, of particles of pure water ice from the E-ring whose source is Enceladus' geysers (Kempf et al., 2010; Juhász and Horányi, 2015; Kempf et al., 2018). Likewise, the overall increase in brightness temperature outward Enceladus may be related to the outward decrease in E-ring flux (Verbicer et al., 2007). However, models also predict the preferential coating of Mimas's trailing side by E-ring particles which should result in a lower $T_{\mathrm{b}}^{\mathrm{disk}}$ on this hemisphere than on the other, opposite to what is observed on Fig. 1.

To confirm these preliminary interpretations and further investigate the inter- and intra-variations of the thermal emission of Saturn's moon, a necessary step is to account for the variations that are due to changes in the physical temperature from one observation to another. Radiometry data were indeed acquired at different seasons and heliocentric distances, local times, latitudes (Table 2) and on surfaces that have different bolometric Bond albedos and likely different thermal properties. In other words, it is crucial to interpret the data based on disk-integrated emissivities rather than disk-integrated brightness temperatures. For such an objective, a thermal model coupled to a radiative transfer model is required as described in the following section.

In addition, for the remainder of the paper, we focus only on the data acquired during distant scans (qualified as "unresolved" in Table 2) as they provide the most reliable $T_{\mathrm{b}}^{\mathrm{disk}}$ values. Indeed, we note that "resolved" observations as well as "stares" acquired with a relatively small beam size tend to lead to higher brightness temperatures than "unresolved" observations. This is partially due to the fact that these former observe a smaller portion of the disk, often devoid of (cold) limbs and centered on (warm) equatorial regions.

Lastly, we highlight that Fig. 1 does not display the $T_{\mathrm{b}}^{\mathrm{disk}}$ value derived from the Enceladus observation EN061-2 1s (see Table 2). This value is especially high (57.8 ± 1.3 K) compared to other measurements on the satellite. Interestingly, it was acquired for a sub-spacecraft point close to the South pole of Enceladus which was found to be anomalously warm both in the infrared (Spencer et al., 2006; Howett et al., 2011) and microwave (Le Gall et al., 2017) domains. Such finding deserves more investigation and is out of scope for this work.

3. Derivation of disk-integrated 2.2-cm emissivities

The disk-integrated emissivity e^{disk} can be deduced from the disk-integrated brightness temperature as follows:

$$e^{\mathrm{disk}} = T_{\mathrm{b}}^{\mathrm{disk}} / T_{\mathrm{eff}}^{\mathrm{disk}} \quad (6)$$

where $T_{\mathrm{eff}}^{\mathrm{disk}}$ is the disk-integrated effective physical temperature (in K). The emissivity is unitless and lies between 0 (for a perfect reflector) and 1 (for a perfect blackbody).

Ostro et al. (2006) use the isothermal equilibrium temperature T_{eq} as a proxy for the effective physical temperature at 2.2 cm with $T_{\mathrm{eq}} = 91.4 \times (1 - A_B)^{1/4}$, where 91.4 K is the equilibrium temperature for a grey body at Saturn's distance from the Sun at the beginning of the Cassini mission and A_B is the bolometric Bond albedo of the satellite. In this work, we propose a more accurate assessment of $T_{\mathrm{eff}}^{\mathrm{disk}}$ that requires a thermal model (section 3.1) and a radiative transfer model (section 3.2).

At a given point on the surface observed with an emission angle θ the effective temperature is computed as follows (see eq. 4.133 in Ulaby, Moore, & Fung (1981)):

$$T_{\mathrm{eff}} = \frac{\int_0^{+\infty} T(z) e^{-\sec\theta' z/\delta_{el}} dz}{\int_0^{+\infty} e^{-\sec\theta' z/\delta_{el}} dz} = \frac{\int_0^{+\infty} T(z) e^{-\sec\theta' z/\delta_{el}} dz}{\delta_{el} \cos\theta'} \quad (7)$$

where z is depth, $T(z)$ the vertical temperature profile in the subsurface, θ' the transmitted angle and δ_{el} the electrical skin depth. δ_{el} can be regarded as proxy for the depth of maximum emission of the radiations received by the radiometer or, in other words, as a proxy for the sounding depth of the instrument. Noting $\varepsilon_r = \varepsilon_r' - j\varepsilon_r''$ the complex relative permittivity of the subsurface, if $\varepsilon_r'' \ll \varepsilon_r'$ then the following equations apply.

$$\sin\theta = \sqrt{\varepsilon_r'} \sin\theta' \quad (8)$$

$$\delta_{el} \approx \frac{\lambda\sqrt{\varepsilon_r'}}{2\pi\varepsilon_r''} \quad (9)$$

where λ is the wavelength of observation (here 2.2 cm). In a water ice regolith, δ_{el} is expected to be of the order of a few meters or even a few tens of meters if the regolith is especially pure (according to Paillou et al., 2008, the electrical skin depth at 2.2 cm in a relatively pure water ice substrate is δ_{el}~4 m).

Equation (7) is valid under the assumption of a homogeneous subsurface and only considers losses by absorption, neglecting scattering in the subsurface. $T_{\mathrm{eff}}^{\mathrm{disk}}$ is derived using equation (5) after substituting T_{b}^{m} by a map of T_{eff} obtained using equation (7) (or equation (11)) on a grid of points on the visible disk. Figure 2 illustrates the different steps of the derivation of e^{disk} for a given observation (acquired over a specific visible disk and at a specific epoch) for a set of varying parameters (namely I and r defined below).

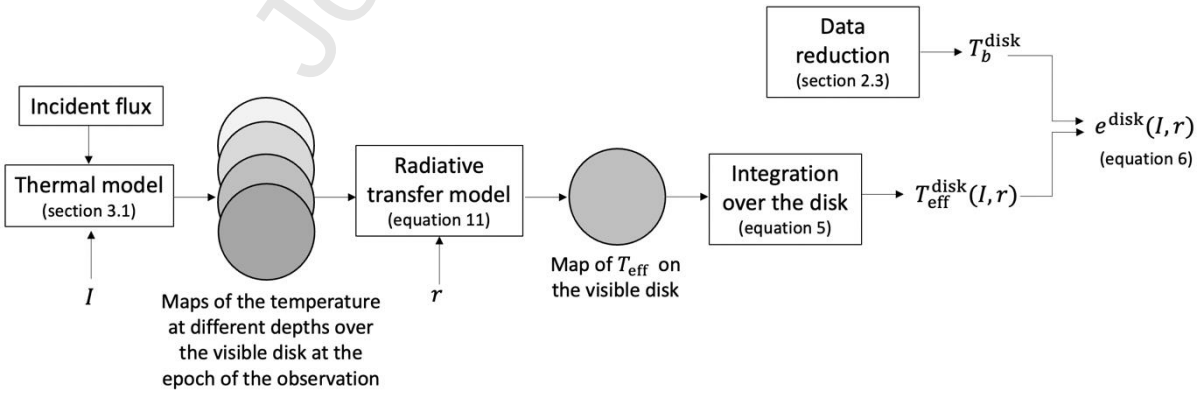

Fig. 2: Derivation of the disk-integrated emissivity e^{disk} for a given icy moon observation and combination of parameters (i.e., a given value of the thermal inertia I and of the ratio of the electrical and thermal skin depths $r = \delta_{el}/\delta_{\mathrm{th}}^{\mathrm{day}}$).

3.1 Thermal model

For each observation, the temperature profiles $T(z)$ at the time of the observation (see Table 3) of different points forming a 10°×10° grid over the visible disk of the targeted satellite is computed using the thermal model initially developed by Ferrari and Leyrat (2006) to simulate Saturn's ring thermal emission and, since then, adapted to icy satellites and used in Le Gall et al. (2014; 2017) and Bonnefoy et al. (2020b).

This model solves in 1D the time-dependent heat equation considering only heat (vertical) transfer by conduction and a subsurface whose thermal properties (in particular thermal inertia) are constant with depth and time. The model assumes no endogenic source of heat. At the surface, a radiative equilibrium is imposed between the outgoing flux (in the IR) and the incident flux (mainly in the optical domain). An infrared emissivity of 1 is assumed for all satellites (as in e.g., Howett et al. 2010). The main source of incident flux is direct solar illumination which varies across the surface and along the satellite's orbit. It is computed using SPICE/NAIF libraries for a grid of points for each satellite, over a full orbit around Saturn, and with a time step small enough to capture the diurnal variations of insolation: from 35 min for Phoebe (which has the shortest rotational period, Table 1) to 9.5 hours for Iapetus (which has the longest rotational period). This corresponds to 200 points per day for Iapetus and only 15 per day for Phoebe for which a compromise has to be found to limit the computational time. For the innermost moons, a short time step is required to properly sample both short duration of the day for synchronous spin and eclipses by Saturn which are here accounted for.

Only a fraction $(1 - A_B)$ of the solar illumination is absorbed by the surface. In the cases of Iapetus and Dione, we use the available bolometric Bond albedo maps (Blackburn et al. 2011; 2012). The map is partial for Dione; it covers only latitudes below 45° but was completed using, on each hemisphere, either the average bolometric Bond albedo of the leading side or that of the (dark) trailing side. At the poles only the leading side value was used since these regions should not be affected by the dark material covering Dione's trailing side. A single albedo value is considered for Mimas (0.49, Howett et al., 2010), Enceladus (0.81, Spencer et al. 2006; Howett et al., 2010), Tethys (0.87, Howett et al., 2010), Rhea (0.60, Howett et al., 2010) and Phoebe (0.1, Flasar et al. 2005, Howett et al., 2010) based on literature. Using Cassini VIMS (mid-infrared) rather than CIRS (thermal infrared) data, Pitman et al. (2010) found slightly different Bond albedos for the inner moons, including leading/trailing dichotomies. To first order, modeled physical temperatures are proportional to $(1\text{-}A_B)^{1/4}$, so higher values of A_B would lead to smaller temperatures and therefore to higher emissivities (and inversely). The consequences of albedo uncertainties are further discussed in section 3.3.

For the inner moons, Saturnshine (sunlight reflected by Saturn onto the satellite) and the thermal infrared emission from Saturn cannot be neglected (in particular near the poles and around the zero longitude meridian); they are computed assuming an effective temperature of 95 K and a bolometric Bond albedo of 0.342 for Saturn (Hanel et al. 1983). These additional sources of heat primarily affect (the sub-Saturn faces of) Mimas, Enceladus and Tethys due to their small orbital radii (Table 1). Yet, Bonnefoy (2020) finds that they also cannot be neglected for Dione and Rhea.

The only varying parameter of the thermal model is the subsurface effective thermal inertia I (in $\mathrm{Jm^{-2}K^{-1}s^{-1/2}}$, hereafter referred to as MKS) which is controlled, above all, by the porosity (or degree of compaction) of the (water-ice dominated) subsurface. The bulk density ρ, thermal conductivity K and heat capacity C of the ground are taken from Klinger (1981) for crystalline

water ice at a temperature of 100 K, namely $\rho = 918$ kg/m^3, $K = 5{,}67$ Wm^{-1}K^{-1} and $C = 839$ Jkg^{-1}K^{-1}.

The 1D heat equation is solved numerically using the semi-implicit Crank-Nicolson algorithm. The discretized spatial step is set to a fifth of the diurnal thermal skin depth $\delta_{th}^{\mathrm{day}}$ which is small enough to sense temperature diurnal variations near the surface, where they are the most pronounced. We recall:

$$\delta_{\mathrm{th}}^{\mathrm{day}}(I) = \frac{I}{\rho C}\sqrt{\frac{P}{\pi}} \quad (10)$$

where P is the rotation period of the targeted satellite (Table 1). For a thermal inertia of 100 MKS, $\delta_{\mathrm{th}}^{\mathrm{day}}$ is typically of the order of 2 cm for Mimas and 20 cm for Iapetus.

Table 3 summarizes the assumptions on the parameters of the thermal model. The temperature profiles $T(z)$ are computed for different values of I (ranging from 10 to 1000 MKS) down to a depth equal to 6 times the seasonal thermal skin depth $\delta_{th}^{\mathrm{season}}$ (computed with equation (10) where P is now the orbital period around the Sun that is about 29.5 years for all satellites). Such a large depth is necessary to capture the seasonal effects which can dominate diurnal variations of the thermal emission in the microwave domain. Indeed, as mentioned before, contrary to infrared wavelengths which sense only the very surface, microwaves can probe depths of several meters or more.

Table 3: Parameters of the thermal and radiative models. Only the subsurface effective thermal inertia I and the ratio r between the electrical and thermal skin depths are allowed to vary. Their variations respectively reflect variations of the subsurface porosity and of its concentration in microwave absorbents which are the key parameters controlling the thermal emission from a water ice subsurface.

Parameters	Values/Range	Comments/References
Subsurface effective thermal inertia I	10 to 1000 Jm^{-2}K^{-1}s$^{-1/2}$	Variations of the effective thermal inertia reflect variations of the ground porosity p. The considered values of I correspond to p ranging from 50 to almost 100%.
Subsurface bulk density ρ	918 kg/m^3	Klinger (1981) for crystalline water ice at a temperature of 100 K.
Subsurface bulk thermal conductivity K	5,67 Wm^{-1}K^{-1}	
Subsurface heat capacity C	839 Jkg^{-1}K^{-1}	
Surface bolometric Bond albedo	Mimas : 0.49 Enceladus : 0.81 Tethys : 0.67 Dione : partial map (0.29-0.8) Rhea : 0.60 Iapetus : global map (0.01-0.41) Phoebe : 0.1	Flasar et al. (2005), Spencer et al. (2006), Howett et al. (2010), Blackburn et al. (2011 ; 2012)
Surface IR emissivity	1	As in Howett et al. (2010)
Saturn's shine and thermal IR emission	Saturn's effective temperature: 95 K Saturn's bolometric Bond albedo: 0.342	Hanel et al. 1983 Saturn's shine and thermal IR emission are taken into account for all the moons except for Iapetus and Phoebe

Subsurface complex permittivity	Real part: $\varepsilon'_r = 1.15$ Imaginary part: ε''_r is allowed to vary by varying $r = \frac{\delta_{el}}{\delta_{th}^{day}}$ from 0.01 to 1000.	ε''_r is the main parameter controlling the electrical skin depth δ_{el} (a proxy for the sounding depth of the radiometer). The wide range of values explored for I and r corresponds to values of $\delta_{el} = r\delta_{th}^{day}(I)$ ranging from 0.1 mm to 100 m and thus to values of ε''_r ranging from 4×10^{-5} to 40. As a reminder expected ε''_r values for water ice at Titan's temperature and 2.2 cm wavelength is 1.3×10^{-3} and ~ 0.02 for compacted organic dust (Paillou et al., 2008) which corresponds to δ_{el} of respectively 4.7 m and 22 cm (equation (9)).

3.2 Radiative transfer model

For each unresolved radiometry observation, the temperature profiles $T(z)$ obtained for a grid of points over the visible disk are then weighted by a radiative transfer function taking into account the viewing geometry and integrated over depth (equation (7)). This requires the introduction of a new variable parameter – the electrical skin depth δ_{el} expressed as a fraction of the diurnal thermal skin depth δ_{th}^{day}.

T_{eff} is therefore computed for different values of I and ratios $r = \delta_{el}/\delta_{th}^{day}$ as follows:

$$T_{eff}(I, r) = \frac{\int_0^{+\infty} T(z, I) e^{-\sec\theta' z/(r\delta_{th}^{day}(I))} dz}{\int_0^{+\infty} e^{-\sec\theta' z/(r\delta_{th}^{day}(I))} dz} \quad (11)$$

Again, we emphasize that this radiative transfer model assumes a scatter-free homogeneous subsurface. Based on the best-fit parameter values found in section 2.3, the real part of the relative permittivity ε'_r (required to compute θ') is set to 1.15. Modifying this value barely affects the results. The imaginary part of the permittivity ε''_r (which describes losses by absorption in the subsurface) is unknown and may vary over several orders of magnitude, depending on the absorptivity and abundance of non-ice contaminants in the satellite regolith. It is the main parameter controlling the electrical skin depth (equation (9)) i.e. the sounding depth of the radiometer. In consequence, varying r for a given value of I is equivalent to varying ε''_r (see Table 3).

Equation (11) leads to a map of the expected effective physical temperatures on the disk visible from the spacecraft for each unresolved observation and combination of parameters (I, r). Such a map can be used to compute T_{eff}^{disk} (using equation (5) after substituting T_b^m by T_{eff}) and then yield $e^{disk}(I, r)$ using equation (6) (see Fig. 2). Before applying equation (6), the T_b^{disk} values derived for two consecutive observations with close sub-spacecraft points (e.g., EN156 10u and EN156 11u, see Table 2) are averaged.

3.3 Emissivity maps

Fig. 3 displays the disk-integrated emissivities obtained for different combinations of thermal inertia and skin depth ratio for each unresolved scan of Mimas, Enceladus, Tethys, Dione, Rhea, Iapetus and Phoebe. A wide range of values was explored both for I (from 10 to 1000 MKS) and r (from 0.01 to 1000). This corresponds to values of δ_{el} ranging from 0.1 mm to 100 m. Some parameter combinations yield a disk-integrated emissivity that exceeds unity which is not physical. Those combinations can be discarded (they are blanked out in Fig. 3, see e.g. Fig. 3f). We mention that similar emissivity maps are shown in Le Gall et al. (2014) for Iapetus, in Le Gall et al. (2017, Supplementary Information) for Enceladus, in Bonnefoy et al. (2020b) for Rhea and in Bonnefoy (2020) for Dione. However, they were obtained with a less complete thermal model. In particular, Saturnshine and infrared thermal emission were neglected in Bonnefoy et al. (2020b) and Bonnefoy (2020). The calibration and reduction of the radiometry

dataset were also updated since these publications. The cases of Mimas, Tethys and Phoebe are presented here for the first time.

Fig. 3 confirms that the 2.2-cm emissivities of the inner moons are significantly smaller than those of the outer moons, irrespective of the assumed values of I and r: the former have disk-averaged emissivities typically in the range 0.5-0.8 against 0.8-1.0 for the latter.

Mimas, Enceladus and Tethys Fig. 3b supports the existence of a large-scale low emissivity anomaly on the leading side of Enceladus observed during EN004 2u and EN050 2u (see section 2.3, Ries and Janssen, 2015). Enceladus's leading/trailing contrast would be even more pronounced if different bolometric Bond albedos had been assumed for the two hemispheres as suggested by Cassini VIMS (near-infrared) observations. Indeed, Pitman et al (2010) report a bolometric Bond albedo of 0.77 $\pm$0.09 for the leading side and 0.93 $\pm$0.11 for the trailing side. By assuming an average and uniform value of 0.81 we may have underestimated (respectively, overestimated) the effective temperature of the leading (respectively, trailing) side and therefore overestimated (respectively, underestimated) its emissivity.
The emissivity of Enceladus's LHT is as low as that of Mimas and Tethys, which is typically in the range 0.50-0.65 (Fig. 3a and Fig. 3c). We stress that these are very low values compared to most other surfaces encountered in the solar system. On Earth, low emissivities are generally associated to the presence of liquid water due to its high (real part of) permittivity (80 against 3 for water ice). Likewise, on Venus, the low emissivity of a number of regions primarily located at high elevations is explained by the presence of very unusual minerals of high permittivity (e.g., ferroelectric substances (Arvidson et al., 1994; Shepard et al., 1994; Treiman et al., 2016)) resulting from the cold trapping of exotic volatile species or yet unidentified weathering reactions (Pettengill et al., 1992, 1996). However, on Saturn's icy moons, in absence of materials of high permittivity, these values rather point to a low-loss regolith where volume scattering dominates. To be efficient, this scattering mechanism requires both the presence of scatterers in the subsurface and multiple opportunities for waves to be scattered. Transparency favors volume scattering and reduces the incoming radiations because it guarantees to the waves a long propagating path in the subsurface and therefore multiple opportunities to be scattered back to depths before reaching the surface.
The transparency of the regoliths of Mimas, Enceladus and Tethys may be, at least partially, due to the deposition at their surface of pure water ice particles emanating from Enceladus's geysers (via the E-ring). Additionally, it could be indicative of the geological youth of the near-surface of these objects as observed on Enceladus's LHT because recent activity likely implies the extrusion of purer water ice from the interior to near-surface. These interpretations are further discussed in section 4.

Dione and Rhea The emissivities of Dione and Rhea are somewhat intermediate between that of the innermost and outermost mid-sized moons (Fig. 3d and 3e) suggesting an increasing concentration of non-ice contaminants in the near-subsurface moving outward from Enceladus and the E-ring. On Dione, the lowest emissivity values are found for DI177, which is centered near the ray crater Creusa (49°N, 76°W, Stephan et al., 2010). The ejecta blanket of this geologically young crater must be water ice rich as the impact that formed it must have brought near the surface purer water ice from the interior. Although the scarcity of data calls for caution, the apparent radiometric coldness of the leading side of Dione in Fig. 1 is therefore probably due to the presence of Creusa crater rather than to a hemispheric-scale emissivity dichotomy. More intriguing, relatively low emissivity values are derived for DI050 on Dione's optically-dark trailing side. The dark coating must be thin on this hemisphere and the measured emissivity

may reflect the exposure of pristine water ice along the scarps of the large fault system (in the so-called "wispy terrain", Smith et al., 1981; Moore, 1984) that covers most of it.
Observations are more numerous on Rhea but none of them is centered on the trailing side of the satellite -- which is, like on Dione, optically-darker than the leading side and covered by extensive scarps and fractures (Moore et al., 1985). Rhea seems to be, in average, less emissive than Dione (unless Rhea's near subsurface has both a small thermal inertia and is very absorptive which is unlikely, Fig. 3e). This is consistent with the higher radar albedos recorded on this satellite (Le Gall et al., 2019) but puzzling as Dione is both closer to Enceladus (and the E-ring) and seemingly more endogenically evolved than Rhea. After active Enceladus, Dione indeed appears to display the youngest surface among Saturn's icy mid-sized satellites with smooth plains, relaxed craters and tectonic patterns (White et al., 2017). The presence of one of the youngest craters in the solar system, Inktomi (14.1°S, 112.1°E, Stephan et al., 2012), on the leading side of Rhea may explain the partially lower emissivity of Rhea (Bonnefoy et al., 2020b). The ejecta blanket of Inktomi indeed extends over hundreds of kilometers and exhibits a very strong water ice signature (Scipioni et al., 2014).
Lastly, we note that the sub-Saturn faces (centered at 0°E longitude) of both Dione and Rhea are associated with somewhat higher emissivity values (see DI016, DI163, RH018 and RH049 in Fig. 3d and 3e). These faces may exhibit peculiar emissivity and/or thermal properties. Alternatively, this observation could be (partially) ascribed to the underestimation of the bolometric Bond albedo of the trailing hemisphere. Especially for Rhea, a uniform bolometric Bond albedo of 0.60 was assumed while Howett et al. (2010) report an averaged albedo of 0.63 on the leading side and 0.57 on the trailing side. Decreasing (respectively, increasing) A_B by 5% on the trailing (resp. leading) side should result in physical temperatures larger (respectively, smaller) by 2% and therefore emissivity reduced (respectively, increased) by 2%.

Iapetus and Phoebe The hemispheric dichotomy of Iapetus is outstanding on Fig. 3f: the leading face exhibits an emissivity >0.85 (see IA00B and IA049 1-2) while the trailing face has a most likely emissivity around 0.7-0.8 (see IA00C and IA049 3-4). Consistent with previous results (Le Gall et al., 2014), this means that the two hemispheres of Iapetus differ from each other in term of bolometric Bond albedo but also in term of 2.2-cm emissivity. This further implies that the dark layer covering Iapetus's leading side is at least one to several decimeters thick and made of a microwave absorbent, which reduces the probing depth and therefore the efficiency of volume scattering in the subsurface. Interestingly, Iapetus's dark terrains 2.2-cm emissivity appears to be close to that of Phoebe (Fig. 3g) which brings another argument in favor of a common nature and origin of their darkening agent. Lastly, on both Iapetus's hemispheres, results rule out parameter combinations with low inertias (<20 MKS) and low electrical skin depths (< 10 cm). On Phoebe, on the contrary, the derived emissivity is barely sensitive to the thermal inertia value mainly due to the fact that this irregular moon is a fast-rotating body (see Table 1). To some extent, this can be regarded as also true for Mimas, Enceladus and Tethys whose rotation periods are smaller than 2 days.

(a) MIMAS

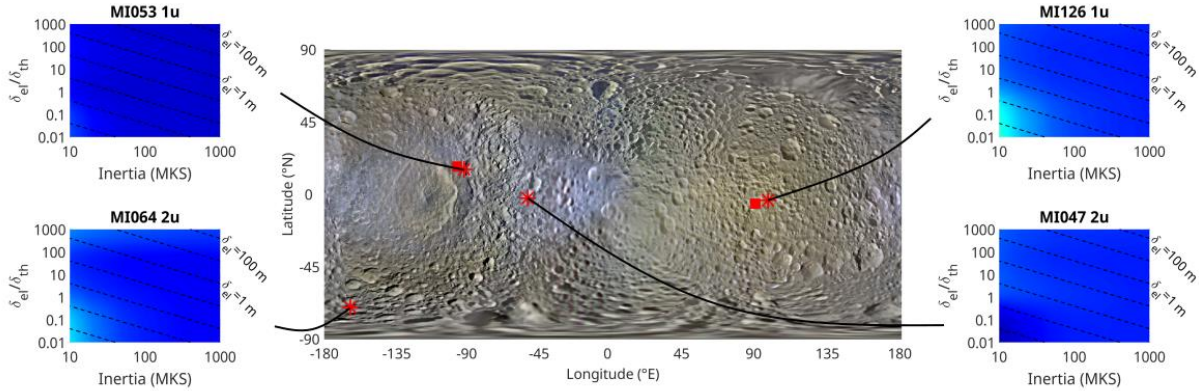

(b) ENCELADUS

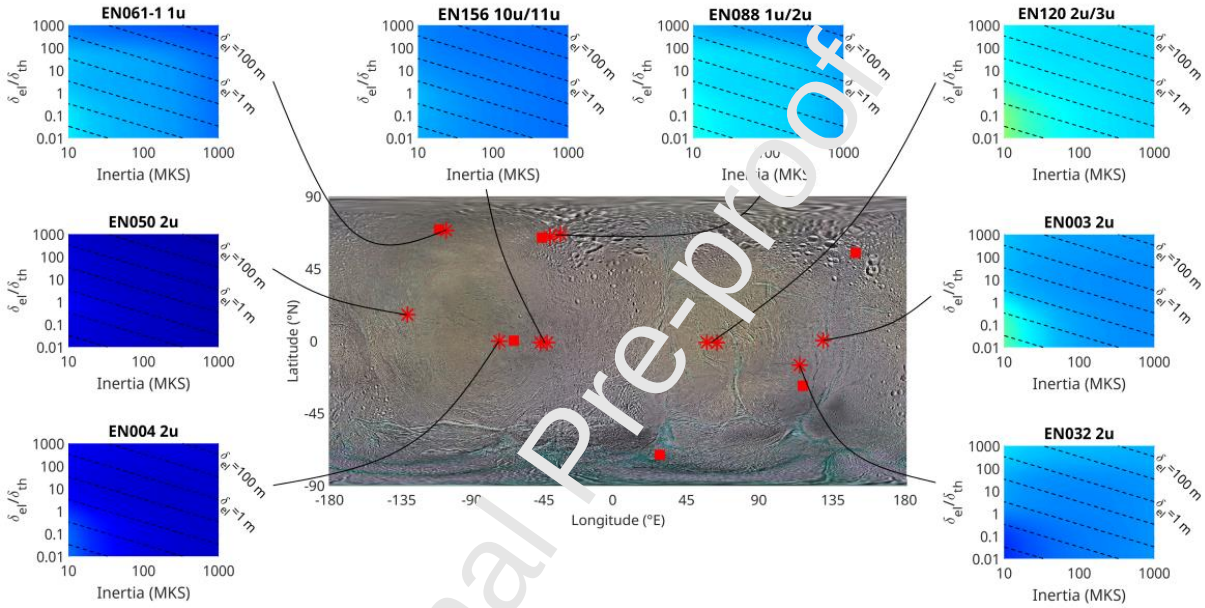

(c) TETHYS

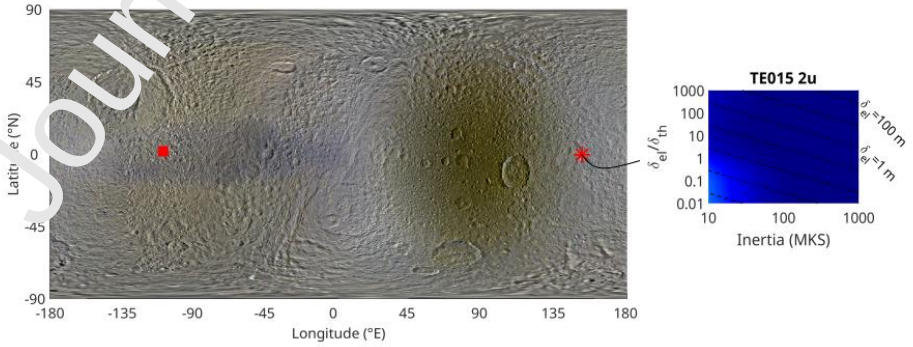

(d) DIONE

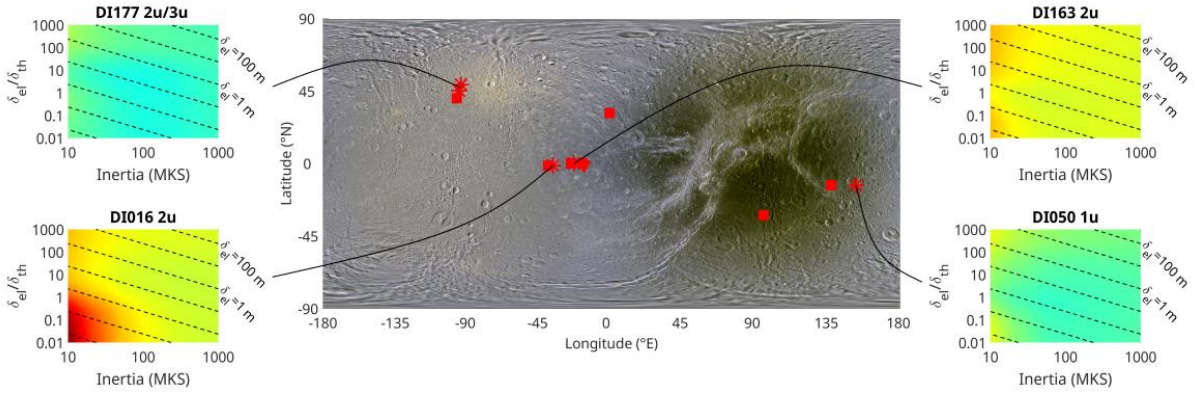

(e) RHEA

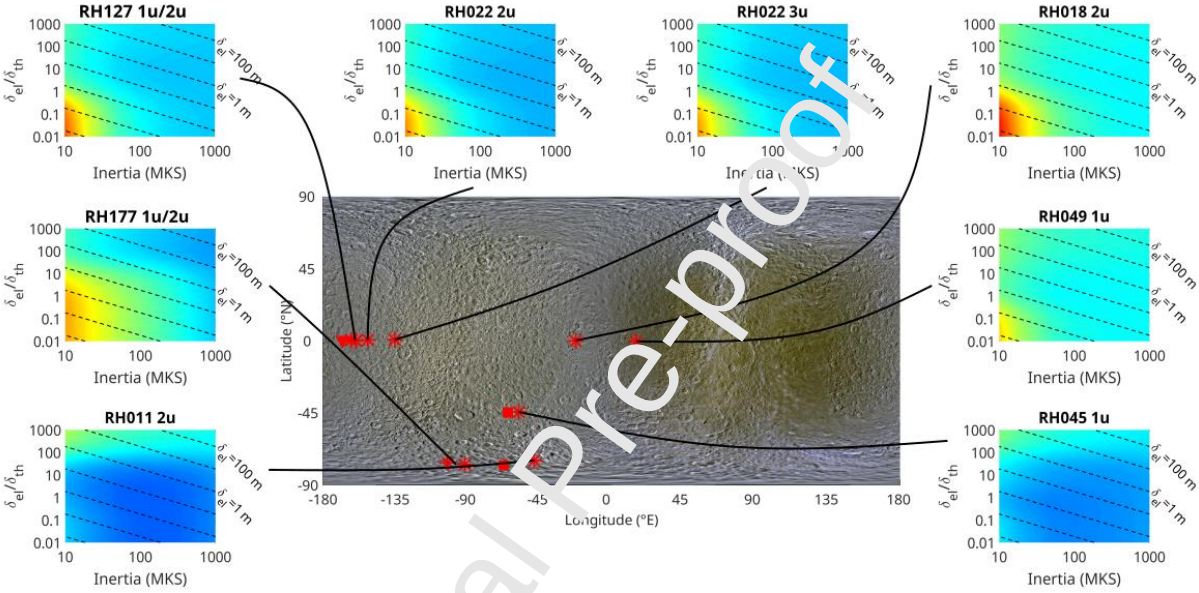

(f) IAPETUS

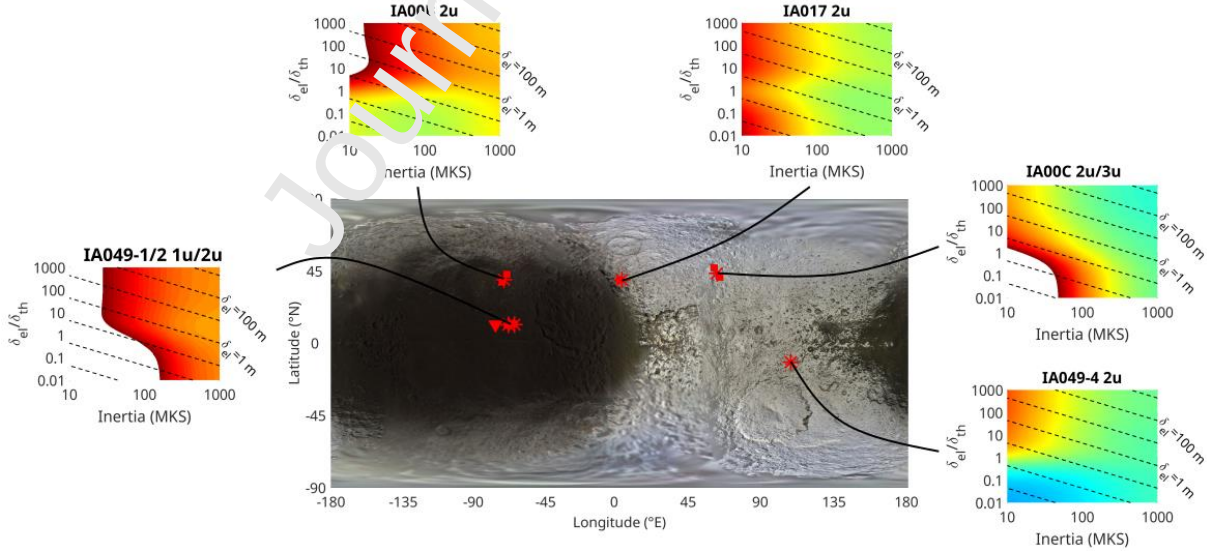

(g) PHOEBE

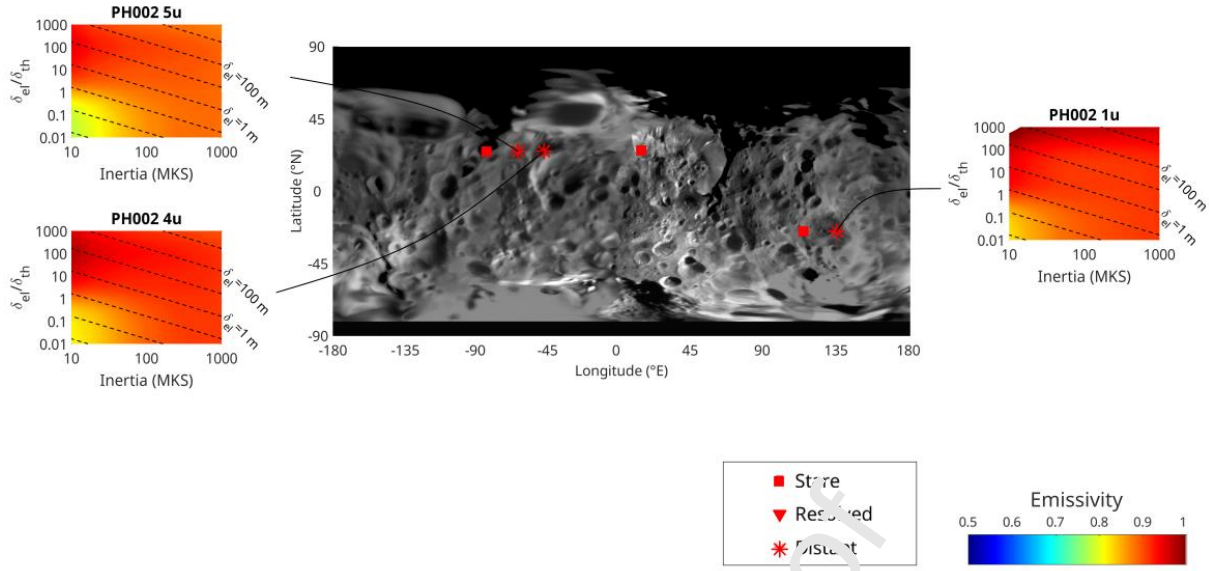

Fig. 3: Disk-integrated emissivities of Mimas (a), Enceladus (b), Tethys (c), Dione (d), Rhea (e), Iapetus (f) and Phoebe (g) as a function of the subsurface thermal inertia I and skin depth ratio r ($r = \delta_{\mathrm{el}}/\delta_{\mathrm{th}}$ with $\delta_{\mathrm{th}} = \delta_{\mathrm{th}}^{\mathrm{day}}$) derived from all unresolved observations of the satellites. Dashed lines indicate the values of the electrical skin depths which are a linear function of I and r (equation (10)). The disk-integrated brightness temperatures of consecutive observations that are very close in term of sub-spacecraft point (e.g., EN156 10u and EN156 11u, see Table 2) have been averaged. Except for Phoebe, the background maps are global enhanced 3-color mosaics obtained by combining Cassini ISS and VIMS datasets: PIA18437 for Mimas, PIA18435 for Enceladus, PIA18439 for Tethys, PIA18434 for Dione, PIA18438 for Rhea and PIA18436 for Iapetus. Phoebe's global map is PIA07775. The sub-spacecraft points of the resolved and stare observations (Table 2) are also indicated on the maps. We recall that the leading hemispheres are centered on -90°E and the trailing ones on 90°E (this does not apply for Phoebe whose rotation is not synchronous).

In the following section, the microwave disk-integrated emissivities derived for each satellite are further analyzed in light of the active radar observations of these objects and of commonly-invoked scattering/emissivity models.

4. Implications of the microwave properties of Saturn's icy satellites

4.1 Comparison with disk-integrated radar albedos

The Cassini RADAR also performed active observations of Saturn's major satellites. Most of them were distant and designed to derive their surface 2.2-cm same-sense (SL) disk-integrated radar albedo $A_{\mathrm{SL}}^{\mathrm{disk}}$. This is the integral over the upper hemisphere of the normalized 2.2-cm radar cross-section measured in the same linear polarization (see Le Gall el al. 2019 for more details). Active and passive distant observations were performed separately but sometimes (especially when they followed each other) observed nearly the same satellite face so that the disk-integrated quantities $A_{\mathrm{SL}}^{\mathrm{disk}}$ and e^{disk} can be directly compared.

Fig. 4 displays the results of this comparison which provides key new constraints for the understanding of the peculiar microwave properties of the surface of Saturnian icy satellites. The case of Titan is added based on disk-integrated emissivities extracted from Sultana et al.,

(2022). The $A_{\mathrm{SL}}^{\mathrm{disk}}$ values for Titan and airless icy satellites are from Le Gall et al., (2019); their respective relative errors are typically of the order of 0.01-0.02 -- i.e. smaller than the size of the markers in Fig. 4. The absolute error on $A_{\mathrm{SL}}^{\mathrm{disk}}$ is about 1.5 dB (1.4 in linear scale) which was estimated adding all known uncertainties on the transmitter power, receiver path losses, receiver gain, and beam solid angle. Rather than single numbers, the ranges of all possible values of e^{disk} as derived in section 3.3 (Fig. 3) are indicated in Fig. 4a. We stress that the highest inferred values of emissivity are unlikely as they were generally obtained under the unrealistic assumption of a very absorptive near-surface (that is for $r = \frac{\delta_{el}}{\delta_{\mathrm{th}}^{\mathrm{day}}} < 1$) while large emission depths are expected for icy subsurfaces. In Fig. 4b (and Fig. 5 and 6), the ranges of possible values for the emissivity are given for more realistic cases where $r = \frac{\delta_{el}}{\delta_{\mathrm{th}}^{\mathrm{day}}} > 1$.

As expected, $A_{\mathrm{SL}}^{\mathrm{disk}}$ and e^{disk} are anti-correlated. Radar reflectivity and thermal radiometry for any surface are indeed related through Kirchhoff's law of thermal radiation which states that the sum of the reflectivity and emissivity of a surface must be unity (see section 4.3 for more details). Of importance, the disk-integrated microwave properties of Saturn's satellites are distributed along a continuous linear trend (dashed line in Fig. 4b), and span a range of values from dark/emissive Titan to bright/cold Enceladus. This strongly suggests that each satellite can be associated to a variable (or a range of values of this variable) along that linear trend. As alluded before, the variable in question is most likely the degree of volume scattering in their respective subsurface which is expected to increase with the degree of transparency of their regolith as well as with their concentration in scatterers. The inter-satellite variations are discussed further below.

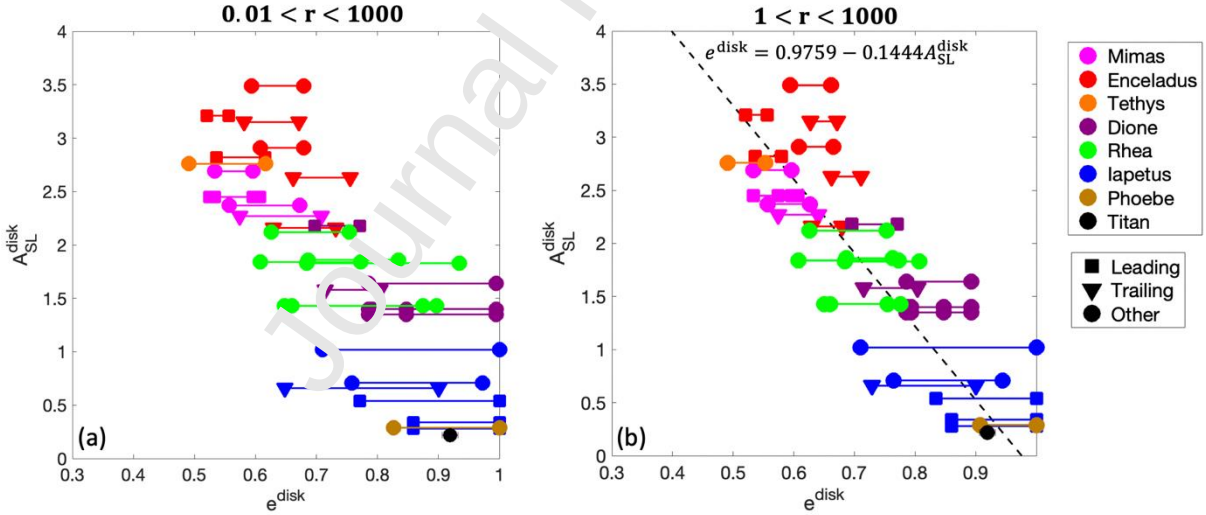

Fig. 4: (a) 2.2-cm same-sense disk-integrated radar albedo (extracted from Le Gall et al., 2019) as a function of the range of possible disk-integrated 2.2-cm emissivity values (as derived from Fig. 3, section 3.3) for Mimas, Enceladus, Tethys, Dione, Rhea, Iapetus and Phoebe. Titan's emissivity value is from Sultana et al. (2022). **(b)** Same as (a) but for the most realistic cases where $r = \frac{\delta_{el}}{\delta_{\mathrm{th}}^{\mathrm{day}}} > 1$ for which the range of possible values for e^{disk} is reduced. A linear law relating e^{disk} to $A_{\mathrm{SL}}^{\mathrm{disk}}$ is indicated (back dashed line); it was obtained fitting (with equal weights) the data points associated with the minimum and maximum emissivity values for each observation.

4.2 Comparison to a model for a particulate medium and interpretation

We here compare the radar and radiometry datasets to the transfer radiative model proposed by Hapke (1990; 2012) for a medium containing efficient scatterers randomly located under the surface. In Hapke (1990; 2012) these scatterers are presented as particles with no specific shape, with size comparable to wavelength and separated by distance of the order or larger than the wavelength. These requirements are somewhat less stringent in Hapke (2012). This model is well suited for cases where multiple/volume scattering in the subsurface largely dominates surface single scattering. It thus applies well to the weakly absorbing (water ice) regoliths of Saturn's icy moons where scatterers could be silicate rocks or voids.

Hapke's model has 3 main parameters:

- $b \in [-1,1]$: A constant describing the medium scattering phase function with $b < 0$ indicating more forward scattering than backscattering and $b > 0$ the opposite.
- $w \in [0,1]$: The single-scattering albedo, which is the ratio of the scattering coefficient to the extinction (or power attenuation) coefficient. This in turn is the sum of the scattering and absorption coefficients. w increases as the absorptivity of the medium decreases and as the concentration of scatterers increases.
- $E_{\mathrm{CBOE}} \in [1,2]$: The Coherent Backscatter Opposition Effect (CBOE) enhancement factor. The CBOE is a phenomenon that occurs in the backscatter direction where waves traveling in opposite directions along the same path interfere constructively thus producing a peak of radiation (Hapke, 1990, Hapke and Blewett, 1991). It is the result of a multiplicity of random scattering events and can enhance the reflectivity by a maximum factor of 2. The CBOE was invoked to explain the radar albedos of the Galilean moons (Black et al., 2004).

Following Hapke (1990), the radar geometric albedo A and thus the total-power (TP) disk-integrated radar albedo $A_{\mathrm{TP}}^{\mathrm{disk}}$ can be expressed as the sum of a single scattering term and a multiple scattering term (that can be enhanced by CBOE) as follows:

$$A_{\mathrm{TP}}^{\mathrm{disk}} = 4A = \frac{w(1+b)}{2} + E_{\mathrm{CBOE}}\left(2r_0 + \frac{2r_0^2}{3} - \frac{w}{2}\right) \quad (12)$$

with $r_0 = \left(1-\sqrt{1-w}\right)/\left(1+\sqrt{1-w}\right)$

In addition, by definition:

$$A_{\mathrm{TP}}^{\mathrm{disk}} = A_{\mathrm{SL}}^{\mathrm{disk}} + A_{\mathrm{OL}}^{\mathrm{disk}} = (1+\mu_L)A_{\mathrm{SL}}^{\mathrm{disk}} \quad (13)$$

where $A_{\mathrm{OL}}^{\mathrm{disk}}$ is the disk-integrated radar albedo in opposite linear (OL) polarization and $\mu_L = A_{\mathrm{OL}}^{\mathrm{disk}}/A_{\mathrm{SL}}^{\mathrm{disk}}$ is the linear polarization ratio. The linear polarization ratio was never measured for Saturn's satellites but observations at 12.6-cm of icy Galilean moons point to values of μ_L around 0.5 (Ostro et al., 1980).

Combining equations (12) and (13) leads to an expression of $A_{\mathrm{SL}}^{\mathrm{disk}}$ as a function of b, w, E and μ_L.

Under the same assumptions as in Hapke (1990), Hapke (2012) proposes the following expression of the directional-hemispherical emissivity viewed at an emission angle θ:

$$e(\theta) = \sqrt{1-w}\,\frac{1+2\cos\theta}{1+2\sqrt{1-w}\cos\theta} \quad (14)$$

Integrating this expression over the disk in the same manner as in equation (5) provides an estimate of e^{disk} as a function of w.

Fig. 5 shows the microwave disk-integrated measurements against predictions from Hapke's model. The implications of this comparison are discussed below.

Inter-satellite variations. Fig. 5 supports the idea that concurrent variations in e^{disk} and $A_{\mathrm{SL}}^{\mathrm{disk}}$ can be primary explained by different values of w i.e., different degrees of transparency of the regoliths and/or different concentrations of scatterers in the subsurface. The smallest values of e^{disk} and the highest values of $A_{\mathrm{SL}}^{\mathrm{disk}}$ are obtained for Enceladus which must therefore be associated with the largest values of w in the Saturnian system. As discussed in section 3.3, to first order, such findings can be mainly explained by the especially pure water-ice regolith of this active world (rather than by a much higher concentration of scatterers than anywhere else, although this may contribute also to the recorded high radar albedos/low emissivities). This further implies that the amount of non-ice contaminants in the near-subsurface likely increases from Enceladus to Titan in the following order: Enceladus, Tethys, Mimas, Rhea, Dione, Iapetus, Phoebe, Titan. In this picture, the subsurface non-ice contaminants do not act as scatterers; they rather consist in dust (or at least particles much smaller in size than the Cassini RADAR wavelength) intimately mixed with water ice. The scattering structures must instead be made of water ice and/or void allowing both efficient scattering and a long penetration depth, that is multiple opportunities for scattering, for radar waves.
In the Saturnian inner system, both radar and radiometry data therefore point to a decrease of Saturnian regolith transparency from Enceladus outward. As argued in Le Gall et al. (2019), the clear correlation between Saturn's moons optical geometric albedos, radar albedos and the optical reflectance profile of the E-ring strongly suggests that the purity of Saturn's inner moon regolith is controlled by the E-ring flux at their position in the Saturnian system. Ultra-pure water ice particles exiting from Enceladus' plumes indeed mantle all satellites orbiting within the E-ring, preferentially on the trailing face inside Enceladus' orbit and on the leading face outside due to the keplerian differential rotation around Saturn. The resulting snow coating must be thick enough - at least a few decimeters - to be detectable in the microwave data; this is much more than predicted by current models of plume-sourced particle deposition (Juhász & Horányi, 2015) but consistent with other observations of depositional features in the inner Saturnian system (Martin et al., 2007; Hirata et al., 2014; Kirchoff and Schenk, 2009).
The only exception to the apparent trend described above is the reversed order of Dione and Rhea (putting aside the data point corresponding to an albedo of 2.1 recorded over the Creusa crater, a region not representative of the rest of Dione). As highlighted before, this exception is all the more puzzling as Dione is seemingly geologically younger than Rhea. To date there is no satisfying explanation for this observation. There may exist a source of dark material preferentially hitting Dione and competing with the deposition of water ice particles from the E-ring. The origin of the dark material covering Dione and Rhea's trailing sides (Fig. 3e and 3f) indeed remains unknown and particles embedded in Saturn's fast rotating magnetosphere are likely more numerous at Dione than at Rhea (Clark et al. 2008). Alternatively and more speculatively, Dione's reduced radar brightness may be related to the fact that Dione is much denser than Rhea (Table 1) and therefore globally poorer in water ice. The ice/rock ratio at the depths sensed by the Cassini radiometer/radar would then have to somehow reflect the interior composition which is only expected if the moon is not fully differentiated. This would be surprising but, on the other hand, we recall that extent of differentiation of the mid-sized Saturnian icy satellites is still poorly constrained (except for Enceladus, Hemingway et al., 2018) and we do note, considering all inner moons except Enceladus, a correlation between the mean density (indicative of the global ice/rock ratio, Table 1) and the 2.2-cm properties of the satellites (indicative of the near-subsurface ice/rock ratio).

Intra-satellite variations Hemispherical and regional differences within each satellite can also be ascribed to different values of w primarily due to different degrees of subsurface transparency at microwaves. For instance, local enhancement of the ice purity and therefore larger values of w are expected on the geologically young Enceladus's South Pole and Leading Hemisphere Terrains or in vicinity of young craters such as Inktomi on Rhea or Creusa on Dione. In contrast, Iapetus's leading side, Phoebe and Titan would be associated with small values of w, consistent with the extensive presence of optically and microwave-dark material onto these surfaces and, which further supports the idea that their dark cover is at least a few decimeters thick. However, the thickness of the dark material covering Iapetus's leading hemisphere most likely does not exceed a few meters as observations from the Arecibo ground-based radar station at 12.6-cm do not show any longitudinal pattern (Black et al., 2004).

Jovian/Saturnian differences The same interpretation applies in the Jovian system where the radar albedo (respectively, emissivity) appears to be correlated (respectively, anticorrelated) with the abundance of water ice in the near subsurface which increases from Callisto to Ganymede to Europa (Ostro et al. 1992). However, as shown in Fig. 5, for a given emissivity, the Jovian moons are generally less radar-bright than the Saturnian ones; Europa, the brightest of these objects, is as bright as Dione (at comparable wavelengths namely 3.5 cm for Europa and 2.2 cm for Dione). According to Hofgartner et al. (2022), which also consider the icy moons in terms of radar circular polarization ratio, this could be due to more forward scattering in the subsurface of Jovian moons (i.e. a lower b in equation (12)) than in that of Saturnian moons. In other words, the scatterers at play in the Jovian subsurfaces would be less efficient retro-reflectors than those in the Saturnian subsurfaces. A different value of b would affect the radar albedo but not the emissivity (equation (14), Fig. 6) and therefore explain why the Saturnian and Jovian satellites' emissivities extend over a similar range while their radar albedos do not. Following this logic, the transparency of Europa's subsurface should be comparable to that of Enceladus' leading side/Tethys/Mimas, while that of Ganymede should be comparable to that of Enceladus (other)/Rhea and that of Callisto to that of Dione/Iapetus.

Hint of an endogenic emission on Enceladus (outside the SPT) and Dione? We note that Enceladus and Dione are somewhat off the general linear trend in Fig. 5 (shifted to the right with respect to the linear law, see also Fig. 4b) with lower limits of their emissivity larger than expected from the trend. One possible explanation is that these lower limits are overestimated because the effective temperatures of Enceladus and Dione are underestimated (see equation (6)). In the case of Enceladus, the assumption of "no internal source of heat" (see section 3.1) is likely incorrect as it appears that the endogenic emission from the moon is not confined to the faults at the source of the plumes. Le Gall et al. (2017) and Howett et al. (2022) indeed respectively reveal thermal anomalies near-by and in-between the "tiger stripes". Recent analysis of the CIRS data even suggests significant endogenic emission in the north polar region (Miles et al., 2022). Though more speculative, the larger inferred emissivities on Dione could also be indicative of current endogenic emission, especially from the sub-Saturn face of the moon. Indeed, after Enceladus, the history of heat flux on Dione as inferred from flexure across tectonic features show levels exceeding that of other Saturnian moons (Hammond et al., 2013; see also Beddingfield et al. (2022) for a review). Better knowledge, especially of surface bolometric Bond of the moons, would help infirm or confirm these interpretations.

Extreme radar brightness The most outstanding feature in Fig. 5 is the inability of the considered model to account for both radiometry and radar observations of most Saturnian moons, even when setting the model parameters to their most extreme values: $E_{\mathrm{CBOE}} = 2$ (maximum CBOE), $b = 1$ (maximum backscatter), $\mu_L = 0$ (absolutely no depolarization

which in unrealistic and in contradiction with observations, Ostro et al., 1980). The predicted radar albedos for a given emissivity are indeed always smaller than those measured for Enceladus, Mimas, Tethys, Dione and Rhea. Even the Jovian observations are barely reproduced. In section 4.3, we further investigate and discuss this discrepancy.

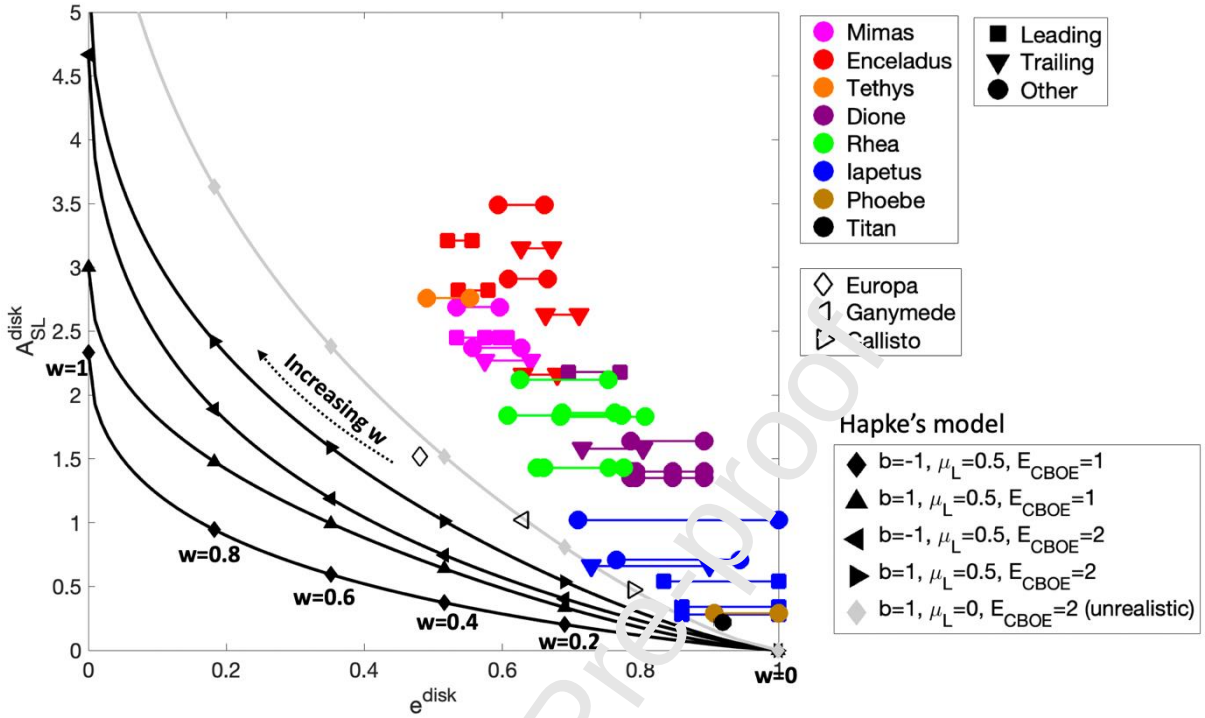

Fig. 5: 2.2-cm same-sense disk-integrated radar albedo (extracted from Le Gall et al., 2019) as a function of the range of possible disk-integrated 2.2-cm emissivity values (as derived from Fig. 3 for $r = \frac{\delta_{el}}{\delta_{\mathrm{th}}^{\mathrm{day}}} > 1$) for Mimas, Enceladus, Tethys, Dione, Rhea, Iapetus, Phoebe and Titan. Black lines display predictions from the Hapke (1990; 2012) model for different sets of parameter values. The grey line is also a model prediction but for an unrealistic value of the linear polarization ratio. Galilean satellite albedos are 3.5-cm values from Ostro et al. (1992), and Galilean satellite emissivities are from de Pater et al. (1984) converted to same-linear sense radar albedo as described in Le Gall et al. (2019, SI).

4.3 Comparison to an empirical purely-random scattering model

In order to further investigate the relationship between radar albedo and emissivity, the radar and radiometry datasets are now compared to an empirical "agnostic" model relying on the simple assumption of an idealized diffuse scattering medium following a cosine power law.

A thorough derivation of Kirchhoff's law of thermal radiation based on the principle of conservation of energy in conventional radar terms is given in Peake (1959). The emissivity $e_p(\theta, \varphi)$ viewed from the (θ, φ) direction (θ and φ are the emission and azimuthal local angles, respectively) at a polarization p is such as:

$$e_p(\theta, \varphi) = 1 - A_p(\theta, \varphi) \quad (15)$$

where $A_p(\theta, \varphi)$ is the hemispherical-directional reflectivity of the medium i.e. the radar albedo obtained by integrating the bidirectional reflectivity of a wave incident from the direction (θ, φ) and with a polarization p over the upper hemisphere. Following Peake (1959) (see also Ulaby et al. 1982), $A_p(\theta, \varphi)$ can be expressed as follows:

$$A_p(\theta,\varphi) = \frac{1}{4\pi}\iint_{\text{upper hemisphere}} \left(\frac{\sigma^0_{pp}(\theta,\varphi;\theta_s,\varphi_s)+\sigma^0_{pq}(\theta,\varphi;\theta_s,\varphi_s)}{\cos\theta}\right)\sin\theta_s d\theta_s d\varphi_s \quad (16)$$

where σ^0_{pp} and σ^0_{pq} are the bistatic cross-sections for the scattering of the incident wave into the direction (θ_s, φ_s) in respective orthogonal polarizations p and q.

The Cassini RADAR, like most radars, only measured the cross-section in the backscattering direction (i.e., for $\theta = \theta_s$ and $\varphi = \varphi_s + \pi$) in same-sense polarization (i.e., σ^0_{pp}). However, Janssen et al. (2011) show that for an idealized diffuse scattering medium following a cosine power law (i.e., $\sigma^0_{pp}(\theta,\varphi;\theta,\varphi) = Kcos^n\theta$), the emissivity viewed from the (θ,φ) direction can be obtained from:

$$e_p(\theta,\varphi) = 1 - \left(\frac{1+\mu_L(\theta,\varphi)}{2n}\right)K \quad (17)$$

where $\mu_L(\theta,\varphi)$ is the linear polarization ratio in the (θ,φ) direction: $\mu_L(\theta,\varphi) = \sigma^0_{pp}(\theta,\varphi;\theta,\varphi)/\sigma^0_{pq}(\theta,\varphi;\theta,\varphi)$. By definition, $\mu_L(\theta,\varphi)$ is between 0 (no depolarization) and 1 (full depolarization). K is the amplitude of the radar backscatter from the surface in the nadir direction. n characterizes the rate at which the radar backscatter decreases with the incidence angle. More specifically, it quantifies how focused diffuse scattering from the surface is.

Then assuming an isotropic polarization ratio (constant μ_L) and accounting for the CBOE (Hapke, 1990), it can be written:

$$e_p(\theta,\varphi) = 1 - \left(\frac{1+\mu_L}{2E_{\text{CBOE}}n}\right)K \quad (18)$$

where E_{CBOE} is between 1 (no coherent backscattering effect) and 2 (maximum coherent backscattering effect) (see section 4.2).

Furthermore, as described in Le Gall et al (2019) (see their SI), the disk-integrated radar albedos $A^{\text{disk}}_{\text{SL}}$ were derived from distant active passes also based on the assumption of empirical purely-diffuse scattering function of the form $cos^n\theta$. Such assumption is supported by the shapes of the measured power spectra which show no hint of specular component (see also Ostro et al., 2006). It results (see equation (2) in the SI of Le Gall et al. 2019):

$$K = \frac{(n+1)}{2}A^{\text{disk}}_{\text{SL}} \quad (19)$$

With a constant μ_L, the emissivity is independent of the emission angle and polarization (i.e., the thermal emission is unpolarized) and the disk-integrated emissivity can be related to the SL disk-integrated radar albedo as follows:

$$e^{\text{disk}} = 1 - \left(\frac{1+\mu_L}{2E_{\text{CBOE}}n}\right)\frac{(n+1)}{2}A^{\text{disk}}_{\text{SL}} \quad (20)$$

Typically, n is encompassed between 1 and 2 (case of a Lambertian medium i.e., a perfectly rough surface that scatters uniformly in all directions) as confirmed by Le Gall et al. (2019) (their SI). As already highlighted in section 4.2, the polarization coefficient μ_L is most likely well above 0 (full conservation of the same-sense linear polarization) since diffuse surfaces are generally also highly depolarizing.

It results from equation (20) that if the medium is such as $n = 1$ and fully depolarizing ($\mu_L = 1$):

$$1 - A^{\text{disk}}_{\text{SL}} \leq e^{\text{disk}} \leq 1 - \frac{A^{\text{disk}}_{\text{SL}}}{2}$$

If the medium is such as $n = 1$ and moderately depolarizing ($\mu_L = 1/2$) or if the medium is Lambertian ($n = 2$) and fully depolarizing ($\mu_L = 1$):

$$1 - \frac{3}{4} A_{\mathrm{SL}}^{\mathrm{disk}} \leq e^{\mathrm{disk}} \leq 1 - \frac{3}{8} A_{\mathrm{SL}}^{\mathrm{disk}}$$

If the medium is Lambertian ($n = 2$) and moderately depolarizing ($\mu_L = 1/2$):

$$1 - \frac{9}{16} A_{\mathrm{SL}}^{\mathrm{disk}} \leq e^{\mathrm{disk}} \leq 1 - \frac{9}{32} A_{\mathrm{SL}}^{\mathrm{disk}}$$

These purely random-scattering models are displayed in Fig. 6 as well as the unlikely case that provides the highest slope for the linear relationship between $A_{\mathrm{SL}}^{\mathrm{disk}}$ and e^{disk}, namely: $n = 2$, $\mu_L = 0, E_{\mathrm{CBOE}} = 2$. It is indeed unlikely that a Lambertian medium would fully conserve the polarization of the incident waves.

The modeled emissivities follow a linear relationship with the radar albedo as observed (Fig. 6). However, except for Iapetus, Phoebe and Titan, the observed linear relationship (see Fig. 4b) exhibits a slope which is a factor of two larger than even the most extreme model considered and a factor of four larger than the most realistic extreme model considered. It thus confirms that the generic scattering models that depend on purely random scattering processes alone cannot explain the combined radiometric and radar distant observations of Mimas, Enceladus, Tethys, Dione and Rhea. The factor of two (or even four) discrepancy between model expectation and observations already allows for maximum CBOE and is well beyond the range that could be accommodated by any conceivable imbalance in the distribution of bistatic polarization, which is assumed to be isotropic in the model. Maybe only a serious underestimation of the absolute uncertainties in both emissivity (typically 0.02, see Janssen et al., 2016) and radar albedo (1.4, see SI of Le Gall et al. 2019) and/or a systematic bias in the radar albedo would accommodate the difference.

A similar discrepancy has been observed locally on Titan, on a radar-bright region called Xanadu (Janssen et al., 2011). Janssen et al. (2011) argue that on Xanadu the mechanism responsible for the enhanced backscatter may be related to the presence of ordered structures on or within the surface. There are many theoretical possibilities for such an enhancement (e.g., a layer of corner cube reflectors); the challenge is to identify those that are geologically plausible for all Saturnian icy satellites. For example, Le Gall et al. (2010) have explained the high radar brightness of some river channels on Titan as due to layers of rounded ice "river pebbles" created by fluvial processes and similar in size to those observed on the Huygens landing site. On Earth, the unusual radar cross sections recorded in the percolation zone of the Greenland ice sheet were modeled as due to ice cylinders/pipes formed by the melting and refreezing of the snow (Rignot et al. 1993; Rignot 1995). Maybe more relevant to the surface of Saturn's atmosphere-less icy satellites, a dense collection of cracks or fissures in the subsurface (due to e.g., impacts or thermal stress) could act as efficient retroreflectors as well as exotic structures such as penitents (proposed for Europa, Hobley et al., 2018) or Sun cups (observed on Hyperion) provided that their dimensions and spacing (and maybe orientation) are appropriate. The role of sintering is also to be examined as it can create "large" subsurface particles and/or layering effects that could enhance volumetric radar backscatter, again provided some geometric constraints that remain to be investigated. The presence of ferroelectric Ice XI which has unknown backscattering properties was invoked (Mitchell et al., 2018); however, it is unclear how it would affect the emissivity. Further modeling and laboratory works are required to place more detailed constraints on these hypotheses. It thus remains that, to date, the exact mechanism(s) responsible for the high radar albedos of Saturn's icy moons is yet to be determined.

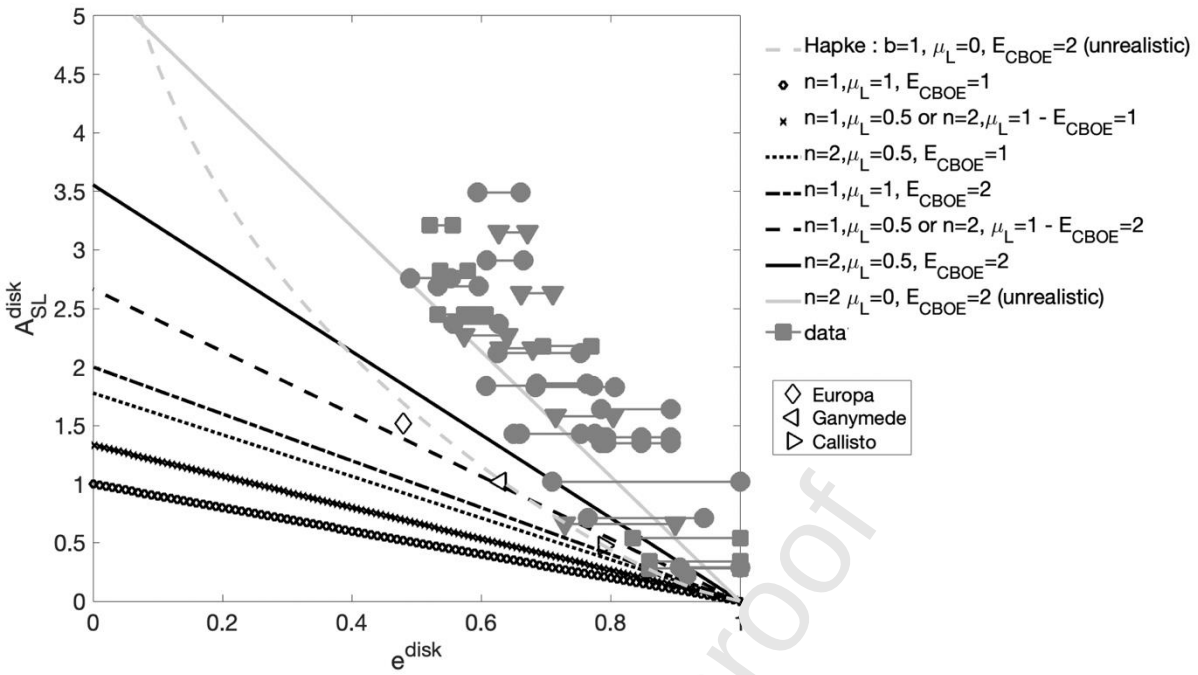

Fig. 6: **:** 2.2-cm same-sense disk-integrated radar albedo (extracted from Le Gall et al., 2019) as a function of the range of possible disk-integrated 2.2-cm emissivity values (as derived from Fig. 4 for $\frac{\delta_{el}}{\delta_{\mathrm{th}}^{\mathrm{day}}} > 1$) for Mimas, Enceladus, Tethys, Dione, Rhea, Iapetus, Phoebe and Titan (grey markers). The dashed grey line displays predictions from the Hapke (1990; 2012) model for the set of (unrealistic) parameter values that provide the largest radar albedos. Black lines display predictions from purely random-scattering models (equation (20)). Galilean satellite albedos are 3.5-cm values from Ostro et al. (1992), and Galilean satellite emissivities are from de Pater et al. (1984) converted in same-linear sense radar albedo as explained in Le Gall et al. (2019, SI).

5. Summary and conclusion

This work presents the complete analysis of all Cassini distant radar and radiometry observations of Saturn's airless satellites. It shows that, to first order, the microwave properties of these objects can be regarded as a measure of the degree of purity of their regolith which were sampled to a considerable depth by the Cassini RADAR at 2.2 cm (at least several meters on Enceladus). An increasing concentration of non-ice contaminant(s) leads to a shallower sounded depth and therefore to the attenuation of the high-order multiple scattering in the subsurface thus resulting in smaller radar albedos and larger emissivities. The variations in concentration of non-ice microwave absorbent material in the subsurface generally mirror that of optically-dark material at the surface. In the Saturnian system it appears to be controlled by the interaction with the dust rings: the E-ring in the inner system, Phoebe's ring in the outer system. It can also be reduced where the terrains are geologically young due to e.g., recent volcanic or tectonic activity or a recent impact. Cassini microwave measurements therefore contain information on both exogenic and endogenic processes affecting Saturn's icy regoliths. The joint analysis of the 2.2-cm radar albedo and thermal emission from Saturn's moons may even have revealed a potential endogenic heat flux emanating from the interior of Enceladus (outside the SPT) and maybe Dione. Fig. 7 summarizes our understanding of the cleanliness of the surface and subsurface of Mimas, Enceladus, Tethys, Dione, Rhea, Iapetus and Phoebe based on both optical (Verbiscer et al., 2007; Hendrix et al., 2018) and microwave observations

(Le Gall et al., 2019; this work). It provides key constraints for retracing the different evolutionary pathway of these objects.

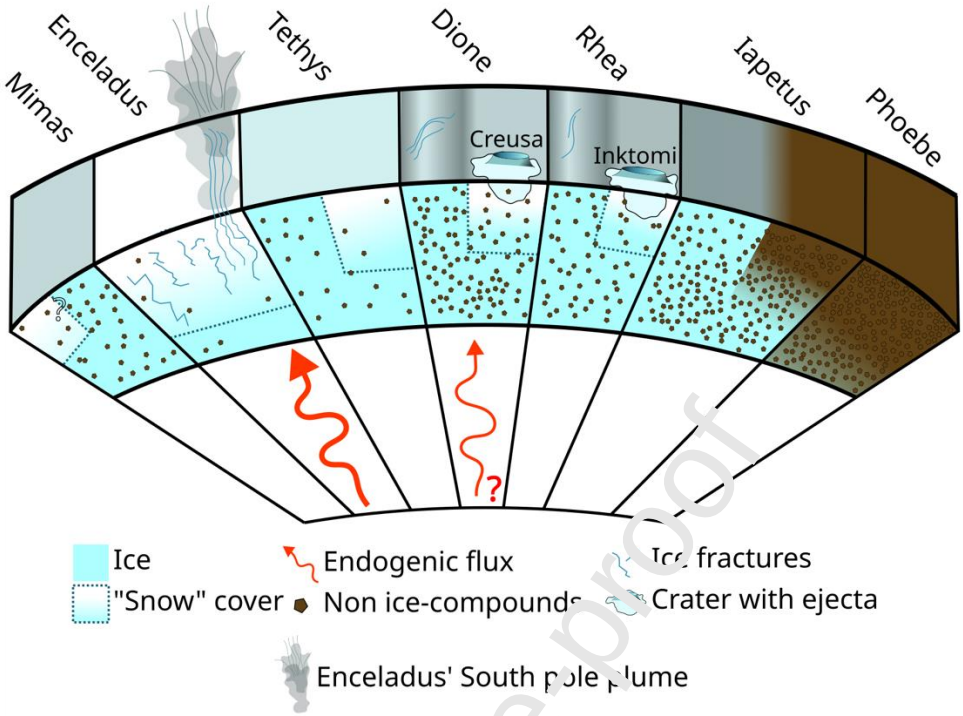

Fig. 7: Diagram of the relative degrees of purity of Saturn's airless icy moons as inferred from optical and microwave observations. The leading sides are on the right and trailing sides on the left. The surface colors represent the optical albedo of the surface (which in some cases includes hemispheric dichotomies, see Verbiscer et al., 2007 and Hendrix et al., 2018). The subsurface color reflects the composition and structure as interpreted from microwave radar/radiometry data. The fresh craters Creusa and Inktomi, the wispy terrains on Dione and Rhea and the tiger stripes on Enceladus which are all associated with lower emissivities than their surroundings, are indicated.

Despite our good first-order understanding of the origins of the observed satellite-to-satellite variations and regional anomalies in terms of microwave properties, no explanation is yet able to accommodate the extreme radar brightness of most Saturnian moons. Indeed, we have shown that, given their surface emissivities, the radar albedos measured over Saturn's inner moons are strongly enhanced, beyond what can be explained by the purely-random scattering models commonly invoked for icy solar system surfaces. It is especially striking how dramatically the radar brightness increases from the Jupiter system to Saturn's one. The radar brightness of Ganymede, Calisto and Europa compared to emissivity is barely within the reach of standard volume-scattering models, but when the Saturnian system enters the picture there is no doubt anymore that a new model paradigm is required.

The extremely high recorded radar albedos may be due to the presence of especially efficient backscattering structures in the subsurface of these objects. We stress that future models should propose geologically plausible structures but also be evaluated based on their ability to explain both the active and passive microwave observations. Understanding the structure of these surfaces is also key to prepare future landings and *in-situ* analysis such as planned for the NASA Enceladus Orbilander mission project (McKenzie et al., 2021).

Lastly, this work demonstrates the value of analyzing active and passive microwave observations in synergy. The comparison of these observations offers an approach to understanding the nature of planetary surfaces that is complementary to that using either radar or radiometry alone. In particular, their joint analysis can reveal thermal anomalies and activity and thus help better assess the habitability of icy moons in the solar system. Cassini observations can also be complemented by measurements from the Earth at other microwave wavelengths i.e., probing different depths. Iapetus is already the target of such an observational campaign; the moon was recently observed at millimetric and centimetric wavelengths by JVLA (Jansky Very Large Array), IRAM NIKA2 and NOEMA (Bonnefoy et al., 2020a; Bonnefoy, 2020). Even if most of these observations are unresolved, they should allow us to put a firm number on the thickness of the dark layer thus bringing key constraints for dynamical models aiming at reproducing dust distribution on Iapetus (Rivera-Valentin et al., 2011).

Acknowledgments

The authors wish to thank the Cassini–Huygens team for the design, development, and operation of the mission. The Cassini–Huygens mission is a joint endeavor of NASA, the European Space Agency (ESA), and the Italian Space Agency (ASI) and is managed by JPL/Caltech under a contract with NASA. The authors also wish to acknowledge the key role played by Steve Ostro in the planning and design of the Cassini RADAR icy satellite observations.

References

Acton, C.H., 1996. Ancillary data services of NASA's navigation and ancillary information facility. Planet. Space Sci. 44 (1), 65–70.

Arvidson R.E. et al., Microwave signatures and surface properties of Ovda. Regio and surroundings, Icarus 112, 171-186 (1994)

Beddingfield, C.B., E. Leonard, R.J. Cartwright, C. Elder and T.A. Nordheim, High Heat Flux near Miranda's Inverness Corona Consistent with a Geologically Recent Heating Event, The Planetary Science Journal, 3:174 (14pp), 2022.

Black, G. J., Campbell, D. B. & Nicholson, P. D. Icy Galilean satellites: Modeling radar reflectivities as a coherent backscattering effect. *Icarus* **151**, 167-180 (2001).

Black, G. J., Campbell, D. B., Carter, L. M., & Ostro, S. J. (2004). Radar detection of Iapetus. Science, 304(5670), 553

Black, G. J., Campbell, D. B. & Carter, L. M. Arecibo radar observations of Rhea, Dione, Tethys, and Enceladus. Icarus 191, 702-711 (2007).

Blackburn, D.G., Buratti, B.J., Ulrich, R., 2011. A bolometric Bond albedo map of Iapetus: Observations from Cassini VIMS and ISS and Voyager ISS. Icarus 212, 329–338.

Bonnefoy L., Lestrade J.-F., Lellouch E., Le Gall A., Leyrat C., Ponthieu N., Ladjelate B., Probing the subsurface of the two faces of Iapetus EPJ Web of Conferences, EDP Sciences, 2020a, 228, pp.00006.

Bonnefoy L., Le Gall A., Lellouch E., Leyrat C., Janssen M., Sultana R., Rhea's subsurface probed by the Cassini radiometer: Insights into its thermal, structural, and compositional properties, Icarus, Elsevier, 2020b, 352, pp.113947

Bonnefoy, Thermal emission from Saturn's icy satellites, Ph.D. Observatoire de ParisMeudon, PSL, 2020.

Buratti, B.J., Hicks, M.D., Tryka, K.A., Sittig, M.S., Newburn, R.L., 2002. Highresolution 0.33–0.92 lm spectra of Iapetus, Hyperion, Phoebe, Rhea, Dione, and D-type asteroids: How are they related? Icarus 155, 375–381.

Butler, B. and M. Gurwell, M.A. (2004). Radio Wavelength Observations of Titan with the VLA, Bulletin of the American Astronomical Society, Vol. 36, p.1075, American Astronomical Society, DPS meeting #36, id.06.04

Campbell, D.B., Black, G.J., Carter, L.M., Ostro, S.J., (2003). Radar evidence for liquid surfaces on Titan. Science, 302, 431–434.

Clark, R. N., Curchin, J. M., Jaumann, R., Cruikshank, D. P., Brown, R. H., Hoefen, T. M., et al. (2008). Compositional mapping of Saturn'ssatellite Dione with Cassini VIMS and implications of dark material in the Saturn system. Icarus, 193(2), 372–386.

Charnoz, S. A. Crida, J.C. Castillo-Rogez, V. Lainey, L. Dones, O. Karatekin, G. Tobie, S. Mathis, C. Le Poncin-Lafitte, J. Salmon, Accretion of Saturn's mid-sized moons during the viscous spreading of young massive rings: Solving the paradox of silicate-poor rings versus silicate-rich moons, Icarus 216 (2011), 535-550.

Crow-Willard, E. N. & Pappalardo, R. T. Structural mapping of Enceladus and implications for formation of tectonized regions. *J. Geophys. Res. Planets* **120**, 928–950 (2015).

Dalle Ore, C.M., Cruikshank, D.P., Clark, R.N., 2012. Infrared spectroscopic characterization of the low-albedo materials on Iapetus. Icarus 221 (2), 735– 743.

de Pater, I., Brown, R.A., Dickel, J.R., 1984. VLA observations of the Galilean satellites. Icarus 57, 93–101.

Elachi, C., Allison, M. D., Borgarelli, L., Encrenaz, P., Im, E., Janssen, M. A., et al., (2004). Radar: The Cassini Titan radar mapper. Space Science Reviews, 115(1), 71–110.

Ferrari, C. and Leyrat, C. (2006). Thermal emission of spherical spinning ring particles - The standard model". A&A 447.2, pp. 745–760.

Flasar, F, Achterberg, R., Conrath, B., Pearl, J., Bjoraker, G., Jennings, D, Romani, P., Simon, A., Kunde, V, Nixon, C., Bézard, B, Orton, G., Spilker, L, Spencer, J, Irwin, P., Teanby, N., Owen, T, Brasunas, J, Segura, M, and Wishnow, E (2005). "Temperatures, Winds, and Composition in the Saturnian System". Science (New York, N.Y.) 307, pp. 1247–51.

Grossman, A.W. and Muhleman, D.O, (1992), Observations of Titan's Radio Light-Curve at 3.5 cm, Bulletin of the American Astronomical Society, Vol. 24, p.954, American Astronomical Society, 24th DPS Meeting, id.12.04

Hagen, N. R., Moullet, A., & Gerwell, M. A. 2014, in American Astronomical Society Meeting Abstracts, Vol. 223, American Astronomical Society Meeting, Abstracts #223, 247.17

Hammond N.P., C.B. Phillips, F. Nimmo and S.A. Kattenhorn, Flexure on Dione: Investigating subsurface structure and thermal history, Icarus 223 (2013), 418-422.

Hanel, R. A., Conrath, B. J., Kunde, V. G., Pearl, J. C., and Pirraglia, J. A. (1983). "Albedo, internal heat flux, and energy balance of Saturn". Icarus 53.2, pp. 262–285

Hapke, B. Coherent backscatter and the radar characteristics of outer planet satellites. *Icarus* **88**, 407-417 (1990).

Hapke, B. & Blewett, D. Coherent backscatter model for the unusual radar reflectivity of icy satellites. Nature 352, 46-47 (1991).

Hapke, B. Theory of Reflectance and Emittance Spectroscopy Ch. 8 (Cambridge Univ. Press, 203 2012).

Hendrix, A. R., Filacchione, G., Paranicas, C., Schenk, P., & Scipioni, F. (2018). Icy Saturnian satellites: Disk-integrated UV-IR characteristics and links to exogenic processes. Icarus, 300, 103–114.

Hemingway, D., Iess, L., Tajeddine, R., Tobie, G. (2018). The interior of Enceladus, in Schenk, P.M., Clark, R.N., Howett, C.J.A., Verbiscer, A.J., Waite, J.H. Enceladus and the icy moons of Saturn. University of Arizona Press.

Hirata, N., Miyamoto, H., & Showman, A. P. (2014). Particle deposition on the Saturnian satellites from ephemeral cryovolcanism on Enceladus. Geophysical Research Letters, 41, 4135–4141.

Hobley, D. E. J., Moore, J. M., Howard, A. D., & Umurhan, O. M. (2018). Formation of metre-scale bladed roughness on Europa's surface by ablation of ice. Nature Geoscience, 11, 901–904

Hofgartner J.D. and K. P. Hand, An icy-satellite radar properties continuum that requires the coherent backscatter effect, 2023, accepted in Nature Astronomy.

Howett, C.J.A., Spencer, J.R., Pearl, J., Segura, M., 2010. Thermal inertia and bolometric Bond albedo values for Mimas, Enceladus, Tethys, Dione, Rhea and Iapetus as derived from Cassini/CIRS measurements. Icarus 206, 573–593

Howett, C. J. A., Spencer, J. R., Pearl, J., Segura & M. High heat flow from Enceladus' south polar region measured using 10–600 cm^{-1} Cassini/CIRS data. *J. Geophys. Res.* **116**, E03003 (2011).

Howett, C., Nimmo, F., and Spencer, J.: Constraining Enceladus' heat flow between its tiger stripes, Europlanet Science Congress 2022, Granada, Spain, 18–23 Sep 2022, EPSC2022-219, https://doi.org/10.5194/epsc2022-219, 2022.

Jaffe, W., Caldwell, J., and Owen, T. (1979). The brightness temperature of Titan at 6 centimeters from the very large array. The Astrophysical Journal, 232:L75.

Jaffe, W., Caldwell, J., and Owen, T. (1980). Radius and brightness temperature observations of Titan at centimeter wavelengths by the Very Large Array. The Astrophysical Journal, 242:806.

Janssen, M. A., Lorenz, R. D., West, R., Paganelli, F., Lopes, R. M., Kirk, R. L., et al., (2009). Titan's surface at 2.2-cm wavelength imaged by the Cassini RADAR radiometer: Calibration and first results. Icarus, 200, 222–239.

Janssen, M.A., Le Gall, A., Wye, L.C., (2011). Anomalous radar backscatter from Titan's surface? Icarus 212, 321–328.

Janssen, M. A., Le Gall, A., Lopes, R. M., Lorenz, R. D., Malaska, M. J., Hayes, A. G., et al. (2016). Titan's surface at 2.18-cm wavelength imaged by the Cassini RADAR radiometer: Results and interpretations through the first ten years of observation. Icarus, 270, 443–459.

Juhász, A., & Horányi, M. (2015). Dust delivery from Enceladus to the moons of Saturn. American Geophysical Union, Abstract 77479

Kempf, S., Beckmann, U., & Schmidt, J. (2010). How the Enceladus dust plume feeds Saturn's E ring. Icarus, 206, 446–457.

Kempf, S., Horányi, M., Hsu, H.-W., Hill, T. W., Juhász, A., & Smith, H. T. (2018). Saturn's diffuse E ring and its connection with Enceladus. In P. M. Schenk, et al. (Eds.), Enceladus and the Icy Moons of Saturn (pp. 195–210). Tucson: University of Arizona.

Klinger, J. (1981). "Some consequences of a phase transition of water ice on the heat balance of comet nuclei". Icarus 47.3, pp. 320–324.

Kirchoff, M. R., & Schenk, P. (2009). Crater modification and geologic activity in Enceladus' heavily cratered plains: Evidence from the impact crater distribution. Icarus, 202(2), 656–668.

Le Gall, A., M.A. Janssen, R.L. Kirk, R.D. Lorenz (2014), Modeling microwave backscatter and thermal emission from fields of linear dunes: Application to Titan. Icarus 230, 198-207.

Le Gall, A., C. Leyrat, M.A. Janssen, G. Choblet, G. Tobie, O. Bourgeois, C. Sotin, A. Lucas, C. Howett, R. Kirk, R.D. West, R.D. Lorenz, A. Stolzenbach, M. Massé, A.H. Hayes, L. Bonnefoy, G. Veyssière and F. Paganelli (2017), Thermally anomalous features in the subsurface of Enceladus's south polar terrain, Nature Astronomy 1-0063.

Le Gall A., West R. D. and Bonnefoy L., Dust and Snow Cover on Saturn's Icy Moons Geophysical Research Letters, 2019, 46 (21), pp. 11747-11755.⟨10.1029/2019GL084218⟩ _

Levenberg, K., 1944. A method for the solution of certain problems in least-squares. Q. Appl. Math. 2, 164–168.

Leyrat, C., Lorenz, R. D. & Le Gall, A. Probing Pluto's Underworld: Ice Temperatures from Microwave Radiometry Decoupled from Surface Conditions. *Icarus* **268**, 50-55 (2016).

Marquardt, D., 1963. An algorithm for least-squares estimation of nonlinear parameters. SIAM J. Appl. Math. 11, 431–444.

Martin, E. S., Kattenhorn, S. A., Collins, G. C., Michaud, R. L., Pappalardo, R. T., & Wyrick, D. Y. (2017). Pit chains on Enceladus signal the recent tectonic dissection of the ancient cratered terrains. Icarus, 294, 209–217.

McKenzie, S.M., et al., The Enceladus Orbilander Mission Concept: Balancing Return and Resources in theSearch for Life, The Planetary Science Journal,2:77(18pp), 2021

Miles, G., Howett, C., and Spencer, J.: Constraining Enceladus' energy emission outside the South Polar Terrain, Europlanet Science Congress 2022, Granada, Spain, 18–23 Sep 2022, EPSC2022-1190, https://doi.org/10.5194/epsc2022-1190, 2022.

Mitchell, K. L., R. Hodyss, M. Choukroun, J. Molaro, A. Le Gall, (2018), Enceladus' brilliant surface 2: Rationalizing Cassini RADAR and optical remote sensing, in Lunar and Planetary Science Conference, 49.

Moeckel, C., Janssen, M. A., and de Pater, I. (2019). "A re-analysis of the Jovian radio emission as seen by Cassini-RADAR and evidence for time variability". Icarus 321, pp. 994–1012.

Moore, J. M. (1984), The tectonic and volcanic history of Dione, *Icarus*, 59(2), 205– 220.

Moore, J. M., Horner, V. M., and Greeley, R. (1985). "The geomorphology of Rhea: Implications for geologic history and surface processes". Journal of Geophysical Research: Solid Earth 90.S02, pp. C785–C795.

Muhleman, D. O., (1990). Radar and Radio Observations of Titan, Bulletin of the American Astronomical Society, 22, 1093.

Muhleman, D. O., Butler, B. J., Slade, M. A., and Grossman, A. W. (1994). Radar Imaging of the Planets Using the Very Large Array. Symposium - InternationalAstronomical Union, 158:457468.

Ostro, S. J. et al. Radar observations of the icy Galilean satellites. Icarus 44, 431-440 (1980).

Ostro, S. J. et al. Europa, Ganymede, and Callisto: New radar results from Arecibo and Goldstone. Journal of Geophysical Research 97, 18227-18244 (1992).

Ostro, S. J. et al. Cassini RADAR observations of Enceladus, Tethys, Dione, Rhea, Iapetus, Hyperion, and Phoebe. Icarus 183, 479-490 (2006).

Ostro, S. J. et al. New Cassini RADAR results for Saturn's icy satellites. Icarus 206, 498-506 (2010).

Paillou, P. et al. Microwave dielectric constant of Titan-relevant materials. Geophys. Res. Lett. 35, L18202 (2008).

Peake, W.H., 1959. Interaction of electromagnetic waves with some natural surfaces. IRE Trans. Antennas Propagation V.7, S324–S329

Pettengill GH, Ford PG, Wilt RJ, 1992. Venus surface radiothermal emission as observed by Magellan. J. Geophys. Res. Planets 97, 13091–13102

Pettengill GH, Ford PG, Simpson RA, 1996. Electrical properties of the Venus surface from bistatic radar observations. Science 272, 1628–1631

Pitman, K. M., Buratti, B. J., and Mosher, J. A. (2010). "Disk-integrated bolometric Bond albedos and rotational light curves of saturnian satellites from Cassini Visual and Infrared Mapping Spectrometer". Icarus 206.2. Cassini at Saturn, pp. 537–560.

Porco, C. C., Helfenstein, P., Thomas, P. C., Ingersoll, A. P., Wisdom, J., West, R., et al. (2006). Cassini observes the active south pole of Enceladus. Science, 311(5766), 1393–1401. https://doi.org/10.1126/science.1123013

Ries, P., 2012. High Frequency Observation of Iapetus on the Green Bank Telescope Aided by Improvements in Understanding the Telescope Response to Wind. Ph.D. Thesis, University of Virginia.

Ries, P. A. and M. A. Janssen, A large-scale anomaly in Enceladus' microwave emission. *Icarus* **257**, 88-102 (2015).

Rignot, E., Ostro, S. J., Van Zyl, J. J., & Jezek, K. C. (1993). Unusual radar echoes from the Greenland ice sheet. Science, 261(5129), 1710–1713.

Rignot, E. Backscatter model for the unusual radar properties of the Greenland Ice sheet. Journal of Geophysical Research 100, 9389-9400 (1995).

Rivera-Valentin, E.G., Blackburn, D.G., Ulrich, R., 2011. Revisiting the thermal inertia of Iapetus: Clues to the thickness of the dark material. Icarus 216, 347–358.

Scipioni, F., Tosi, F., Stephan, K., Filacchione, G., Ciarniello, M., Capaccioni, F., and Cerroni, P. (2014). "Spectroscopic classification of icy satellites of Saturn II: Identification of terrain units on Rhea". Icarus 234, pp. 1–16

Shepard, M.K., Arvidson, R.E., Brackett, R.A., and Fegley Jr., B., Geophys. Res. Lett. Vol 21, Issue 6, pp.
469-472 (1994) doi:10.1029/94GL00392

Smith, B. A., et al. (1981), Encounter with Saturn: Voyager 1 imaging science results, *Science*, 212(4491), 163– 191.

Spencer, J. R. *et al*. Cassini encounters Enceladus: background and the discovery of a south polar hot spot. *Science* **311**, 1401–1405 (2006).

Stephan, K., Jaumann, R., Wagner, R., Clark, R. N., Cruikshank, D. P., Giese, B., Hibbitts, C. A., Roatsch, T., Matz, K.-D., Brown, R. H., Filacchione, G., Cappacioni, F., Scholten, F., Buratti, B. J., Hansen, G. B., Nicholson, P. D., Baines, K. H., Nelson, R. M., and Matson, D.L. (2012). "The Saturnian satellite Rhea as seen by Cassini VIMS". Planetary and Space Science 61.1, pp. 142–160

Sultana, R., Le Gall, A., Bonnefoy, L., and Butler, B.: Insights from Cassini distant radiometry observations of Titan's surface, Europlanet Science Congress 2022, Granada, Spain, 18–23 Sep 2022, EPSC2022-807, https://doi.org/10.5194/epsc2022-807, 2022.

Thomas, P.C., 2010. Sizes, shapes, and derived properties of the saturnian satellites after the Cassini nominal mission. Icarus 208, 395–401

Treiman AH, Harrington E, Sharpton V, 2016. Venus' radar-bright highlands: different signatures and materials on Ovda Regio and on Maxwell Montes. Icarus 280, 172–182.

Ulaby, F.T., Moore, R.K., Fung, A.K., 1981. Microwave Remote Sensing: Active and Passive. Microwave Remote Sensing Fundamentals and Radiometry, vol. I. Addison-Wesley, Advanced Book Program, Reading, Massachusetts, 456p.

Ulaby, F. and Long, D. (2015). Microwave Radar and Radiometric Remote Sensing.

Verbiscer, A.J., Skrutskie, M.F., Hamilton, D.P., 2009. Saturn's largest ring. Nature 461, 1098.

Verbiscer, A., French, R., Showalter, M. & Helfenstein, P. Enceladus: Cosmic Graffiti Artist Caught in the Act. Science 315, 815 (2007).

White, O. L., Schenk, P. M., Bellagamba, A. W., Grimm, A. M., Dombard, A. J., and Bray, V. J. (2017). "Impact crater relaxation on Dione and Tethys and relation to past heat flow". Icarus 288, pp. 37–52

Wye, L., 2011. Radar Scattering from Titan and Saturn's Icy Satellites using the Cassini Spacecraft. Ph.D. Thesis, Stanford University, Faculty of Engineering. p. 316.

Zebker, H. A., Y. Gim, P. Callahan, S. Hensley, R. D. Lorenz, the Cassini RADAR Team, (2009), Analysis and interpretation of Cassini Titan radar altimeter echoes, Icarus, 200:240–255.

Zhang, Z., Hayes, A. G., Janssen, M. A., Nicholson, P. D., Cuzzi, J. N., de Pater, I., Dunn, D. E., Estrada, P. R., and Hedman, M. M. (2017). "Cassini microwave observations provide clues to the origin of Saturn's C ring". Icarus 281, pp. 297–321.

- Joint analysis of Cassini RADAR active and passive observations of Saturn's moons
- Microwave signatures of icy satellites primarily reflect the purity of their regolith
- Youngest surfaces and surfaces closest to E-ring are the cleanest
- Hint of an endogenic source of heat outside Enceladus' South Pole
- Purely-random scattering models fails to explain radar albedos, given emissivities